



# AMERICAN METEOROLOGICAL SOCIETY

*Bulletin of the American Meteorological Society*

## **EARLY ONLINE RELEASE**

This is a preliminary PDF of the author-produced manuscript that has been peer-reviewed and accepted for publication. Since it is being posted so soon after acceptance, it has not yet been copyedited, formatted, or processed by AMS Publications. This preliminary version of the manuscript may be downloaded, distributed, and cited, but please be aware that there will be visual differences and possibly some content differences between this version and the final published version.

The DOI for this manuscript is doi: 10.1175/BAMS-D-17-0180.1

The final published version of this manuscript will replace the preliminary version at the above DOI once it is available.

If you would like to cite this EOR in a separate work, please use the following full citation:

Albrecht, B., V. Ghatge, J. Mohrmann, R. Wood, P. Zuidema, C. Bretherton, C. Schwartz, E. Eloranta, S. Glienke, S. Donaher, M. Sarkar, J. McGibbon, A. Nugent, R. Shaw, J. Fugal, P. Minnis, R. Paliknoda, L. Lussier, J. Jensen, J. Vivekanandan, S. Ellis, P. Tsai, R. Rilling, J. Haggerty, T. Campos, M. Stell, M. Reeves, S. Beaton, J. Allison, G. Stossmeister, S. Hall, and S. Schmidt, 2018: Cloud System Evolution in the Trades—CSET Following the Evolution of Boundary Layer Cloud Systems with the NSF/NCAR GV. *Bull. Amer. Meteor. Soc.* doi:10.1175/BAMS-D-17-0180.1, in press.



1 **Cloud System Evolution in the Trades—CSET**

2 *Following the Evolution of Boundary Layer Cloud Systems with the NSF/NCAR GV*

3  
4 Bruce Albrecht, Virendra Ghate, Johannes Mohrmann, Robert Wood, Paquita Zuidema,  
5 Christopher Bretherton, Christian Schwartz, Edwin Eloranta, Susanne Glienke, Shauna  
6 Donaher, Mampi Sarkar, Jeremy McGibbon, Alison D. Nugent, Raymond A. Shaw, Jacob Fugal,  
7 Patrick Minnis, Robindra Paliknoda, Louis Lussier, Jorgen Jensen, J. Vivekanandan, Scott Ellis,  
8 Peisang Tsai, Robert Rilling, Julie Haggerty, Teresa Campos, Meghan Stell, Michael Reeves,  
9 Stuart Beaton, John Allison, Gregory Stossmeister, Samuel Hall, Sebastian Schmidt

10  
11 **Affiliations:**

12 Albrecht, Zuidema, Sarkar—Dept. Atmospheric Science; Univ. Miami; Bretherton, Wood,  
13 Mohrmann, McGibbon—Dept. Atmos. Sciences, Univ. Washington; Eloranta—Univ.  
14 Wisconsin; Glienke, Shaw—Atmos. Sci. Program, Michigan Technological Univ.;  
15 Donaher—Emory University; Nugent—Dept. Atmospheric Sciences, Univ. Hawaii at  
16 Mānoa; Schmidt—Univ. of Colorado; Fugal—Max Plank Institute of Chemistry; Ghate,  
17 Schwartz—Argonne National Laboratory; Minnis, Palikonda —Science Systems and  
18 Applications, Inc., NASA Langley Research Center; Lussier, Jensen, Vivekanandan, Ellis,  
19 Tsai, Haggerty, Reeves, Beaton, Allison, Stossmeister, Hall, Stell—Earth Observing  
20 Laboratory, NCAR; Campos—Atmospheric Chemistry Observations and Modeling  
21 Laboratory, NCAR

22  
23 **Corresponding Author E-Mail:** Bruce Albrecht, [balbrecht@miami.edu](mailto:balbrecht@miami.edu)

1  
2  
3  
4  
5

## **Capsule Summary**

The evolution of the boundary layer aerosol, cloud, precipitation, and thermodynamic structures along trajectories within the north-Pacific trade-winds was investigated using the NSF NCAR Gulfstream V.

1 **Abstract**

2

3 The Cloud System Evolution in the Trades (CSET) study was designed to describe and

4 explain the evolution of the boundary layer aerosol, cloud, and thermodynamic structures along

5 trajectories within the north-Pacific trade-winds. The study centered on 7 round-trips of the NSF

6 NCAR Gulfstream V (GV) between Sacramento, CA and Kona, Hawaii between 7 July and 9

7 August 2015. The CSET observing strategy was to sample aerosol, cloud, and boundary layer

8 properties upwind from the transition zone over the North Pacific and to resample these areas

9 two days later. Global Forecast System forecast trajectories were used to plan the outbound flight

10 to Hawaii with updated forecast trajectories setting the return flight plan two days later. Two key

11 elements of the CSET observing system were the newly developed HIAPER Cloud Radar (HCR)

12 and the High Spectral Resolution Lidar (HSRL). Together they provided unprecedented

13 characterizations of aerosol, cloud and precipitation structures that were combined with *in situ*

14 measurements of aerosol, cloud, precipitation, and turbulence properties. The cloud systems

15 sampled included solid stratocumulus infused with smoke from Canadian wildfires, mesoscale

16 cloud-precipitation complexes, and patches of shallow cumuli in very clean environments. Ultra-

17 clean layers observed frequently near the top of the boundary layer were often associated with

18 shallow, optically thin, layered veil clouds. The extensive aerosol, cloud, drizzle and boundary

19 layer sampling made over open areas of the Northeast Pacific along 2-day trajectories during

20 CSET is an unprecedented resource for modeling studies of boundary layer cloud system

21 evolution and its governing physical processes.

## 1           **1. Introduction and Motivation**

2           Boundary-layer clouds in the form of stratocumulus and small marine cumulus are the  
3 most frequently observed cloud types over the Earth's oceans, are the most abundant types  
4 globally (Norris, 1998) and have an important impact on the Earth's radiation budget (Hartmann  
5 and Short 1980). The energy and moisture fluxes associated with these clouds are critical in  
6 maintaining the thermodynamic structure of the lower troposphere. Thus, both the turbulent  
7 mixing and the radiative impact on the surface associated with marine boundary layer (MBL)  
8 clouds need to be adequately parameterized in large-scale models (Bony and Dufresne, 2005).  
9 The inadequate representation of MBL cloud processes in large-scale models continues to be a  
10 major contributor to model uncertainties in cloud feedback representations-- particularly in  
11 subtropical anticyclone regions (Zhang et al. 2005, Wyant et al. 2010, Teixeira et al. 2011, Soden  
12 and Vecchi, 2011).

13           The stratocumulus (Sc) regimes associated with the eastern flank of the subtropical  
14 anticyclones evolve into fair-weather cumulus (Cu) regimes in the persistent trade winds  
15 associated with the anticyclones. The high albedo and large areal extent of Sc induce a  
16 significant reduction in surface solar heating (e.g., Hartmann et al, 1992; Klein and Hartmann  
17 1993). Cumuli, on the other hand, play a fundamental role in the regulation of ocean surface  
18 evaporation and convergence of moisture into deep convective regions (e.g., Tiedtke 1989,  
19 Neggers et al. 2007), and therefore the global hydrological cycle. The transition from shallow,  
20 cloud-topped MBLs in the cool subtropics to broken trade cumulus over the warm tropics  
21 (Bretherton and Wyant 1997, Wyant et al. 1997, Sandu and Stevens 2011) occurs over all  
22 subtropical ocean basins and sets the climatological distribution of cloud cover (Albrecht et al.  
23 1995). In the Sc-Cu transition, the MBL evolves from a well-mixed, single layer topped with

1 extensive clouds under a sharp inversion, into a deeper, vertically-stratified structure containing  
2 cumulus clouds with greatly reduced cover capped by a weaker and more diffuse inversion.

3         Cloud top entrainment is one of the key processes driving the stratocumulus-to-cumulus  
4 transition. The MBL deepening associated with entrainment causes decoupling: the separation of  
5 the MBL into two distinct layers with limited exchange between them, an exchange that is  
6 mediated by the cumulus rooted in the lower surface-based mixed layer. Decoupling starves the Sc  
7 of their surface moisture source while the continuing entrainment of dry air into the MBL due to  
8 the more energetic cumulus plumes leads to the breakup of the StCu. They are replaced by broken  
9 Cu whose tops are more variable, with a greater spread of cloud top height and fewer reaching the  
10 inversion. Cloud top entrainment profoundly impacts the type and coverage of clouds within the  
11 MBL because it plays such an important role in the MBL moisture, heat and momentum budgets  
12 (Lilly 1968, Bretherton and Wyant 1997, Wyant et al. 1997, Stevens 2002, Stevens et al. 2002). In  
13 addition, cloud top entrainment controls how MBL clouds respond to increased greenhouse gases  
14 (Caldwell and Bretherton 2009) and atmospheric aerosols (Ackerman et al. 2004, Wood 2007,  
15 Bretherton et al. 2007).

16         Precipitation can also hasten the stratocumulus-to-cumulus transition (Yamaguchi et al.  
17 2017, Abel et al., 2017). Both the cloud depth and the aerosol CCN concentrations can impact the  
18 initiation of precipitation. Thus entrainment growth of the boundary layer depth is a factor in the  
19 development of drizzle. The subsequent removal of aerosols by the precipitation maintains an  
20 environment of enhanced precipitation susceptibility. This feedback between the aerosol removal  
21 and the precipitation enhancement increases the rate at which the cloudiness can decrease  
22 (Yamaguchi et al. 2017). Thus cloud-aerosol-precipitation interactions can play an important role  
23 in the rate at which the transition occurs.

1           Cloud System Evolution in the Trades (CSET) was developed to describe and explain the  
2 evolution of the MBL aerosol, cloud, and thermodynamic structures along trajectories within the  
3 north-Pacific trade-winds using the NSF/NCAR Gulfstream V (GV, formerly known as  
4 HIAPER--High Performance Instrumented Airborne Platform for Environmental Research) on  
5 flights between California and Hawaii. The long range and endurance of the NSF GV allowed  
6 for the sampling of air masses on low-level trajectories extending from California to Hawaii and  
7 then a re-sampling of these same air masses on the return flight two days later.

8           The stratocumulus-trade cumulus transition is often sharply defined, as shown in Fig. 1.  
9 The upstream part of the transition was arguably first examined with five NCAR Electra flights  
10 undertaken in 1975 and documented in Brost et al. (1982a; 1982b) and Albrecht et al. (1985). The  
11 Atlantic Stratocumulus Transition Experiment (ASTEX; Albrecht et al., 1995a) brought new cloud  
12 remote sensors to the field, as well as an explicit Lagrangian sampling approach. Two Lagrangian  
13 experiments each tracked air masses for 36-48 hours using instrumented aircraft (Bretherton and  
14 Pincus, 1995; Bretherton et al., 1995). The ASTEX Lagrangian studies, however, were not made  
15 in classic trade-wind flow conditions and lacked the aircraft-based lidar and radar observations  
16 needed to provide a detailed mapping of cloud and precipitation structures.

17           More recent regional observational and modeling studies have also focused on the MBL  
18 cloud, aerosol, and precipitation structures in cloud regimes associated with the transition.  
19 During the VAMOS Ocean-Cloud-Atmosphere-Land Study Regional Experiment (VOCALS-  
20 REx, 2008) a comprehensive study was made of the aerosol, cloud, and precipitation properties  
21 of stratocumulus clouds in the southeastern Pacific (Wood et al., 2011a; Mechoso et al., 2014).  
22 The observational and modeling studies focused on the stratocumulus structures extending  
23 westward from the west coast of Chile. The VOCALS studies have brought important new

1 insight into the extreme aerosol-cloud interactions associated with Pockets of Open Cells (POCs)  
2 and the role of mesoscale organizations in those interactions (Wood et al, 2011b; Berner et al.,  
3 2011; Kazil et al., 2012; Wang et al., 2010; Berner et al., 2013) In addition, VOCALS provided  
4 a comprehensive description of the aerosol, cloud, precipitation and MBL structures as the MBL  
5 deepens along 20 °S for ~1500 km westwards from the Chilean coast (Bretherton et al., 2010a).  
6 The VOCALS results provide an important baseline for comparing the microphysical and  
7 macrophysical structure of the clouds sampled during CSET.

8         VOCALS did not extend into the trade-wind cumulus regime downwind of the main Sc  
9 deck. Much of the early observational work on small cumuli in the trade wind boundary layer  
10 was conducted using *in situ* aircraft observations. But there are inherent limitations to this  
11 approach since the volume sampled during an aircraft penetration is relatively small and it is  
12 difficult to study the time evolution of the vertical structure. Furthermore, it is difficult to  
13 determine exactly where in the cloud the measurements are being made and what stage of the  
14 cloud life cycle is being sampled. During the Rain in Cumulus over the Ocean (RICO; Rauber et  
15 al., 2007) field campaign some important issues were addressed concerning aerosol-cloud  
16 interactions (e.g. Gerber et al. 2008); but the RICO aircraft measurements did not benefit from  
17 good cloud radar observations. During the Barbados Aerosol Cloud Experiment (BACEX, 2010)  
18 *in-situ* cloud observations in fair weather cumulus clouds were made with the CIRPAS Twin  
19 Otter research aircraft (Jung et al.,2012) and with an upward-pointing Frequency Modulated  
20 Continuous Wave (FMCW) cloud radar. The RICO and BACEX observations provided insight  
21 into entrainment and precipitation processes in liquid-only cumulus clouds (e.g., Nuijens et al.,  
22 2009; Minor et al., 2012; Zuidema et al., 2012a) and provide a background for the CSET  
23 observations in the fair-weather cumulus regions sampled.

1           Although recent field programs have advanced our understanding of processes operating  
2 in the two cloud regimes central to CSET, they have not directly addressed the stratocumulus to  
3 trade cumulus transition. A recent study, MAGIC (the Marine ARM GPCI Investigation of  
4 Clouds), involved ship-borne measurements from a container ship that made regular transects  
5 between Los Angeles and Hawaii from October 2012 to September 2013 using the Department  
6 of Energy's (DOE's) Atmospheric Radiation Measurement program (ARM) Mobile Facility  
7 (Zhou et al., 2015). In addition to *in situ* observations, the clouds above the ship were sampled  
8 using lidar and radar observations in both the stratocumulus and the trade cumulus regime.  
9 Although the cloud transition is well defined in some transects, the slow movement of the ship  
10 limits the usefulness of these observations for Lagrangian studies.

11           The subtropical NE Pacific stratocumulus to cumulus transition sampled during CSET  
12 flights has long been a canonical modeling challenge. Two benchmark cases of Sc-Cu transition  
13 have been used for international modeling inter-comparison efforts as part of the Global  
14 Atmospheric System Study (GASS) and its predecessor, GCSS. The first of these was from the  
15 1992 NE Atlantic ASTEX project described previously (Bretherton et al. 1995,1999; van der  
16 Dussen et al. 2013). The second was a satellite derived composite (Sandu et al. 2010; de Roode  
17 et al. 2016) of several thousand Lagrangian trajectories based on MODIS cloud observations  
18 with trajectories based on ECMWF reanalyses. Neither case includes a good accompanying set  
19 of aerosol observations in or above the boundary layer or the robust statistics on horizontal cloud  
20 and precipitation inhomogeneity that a cloud radar and lidar combination can provide (e. g.  
21 Bretherton et al. 2010b; Wood et al. 2011b).

22           LES models have become a robust tool for Lagrangian simulations of subtropical  
23 cloudiness transitions, but there are few good datasets for comprehensively testing these

1 simulations. In particular, we lack adequate observations of the coupled evolution of aerosol,  
2 cloud droplet number concentration and precipitation during such transitions. The MAGIC AMF  
3 deployment provided a ship-based perspective on this problem (McGibbon and Bretherton, 2017;  
4 Zhou et al., 2015), but the long range of the GV allows *in situ* measurements of aerosols and  
5 cloud microphysics, including interactions with the free troposphere, across the entire transition.  
6 By resampling the same boundary-layer air masses on the return flights as the outbound flights,  
7 the measurements can naturally be compared with the Lagrangian LES that have proved to be  
8 valuable for constructing and analyzing better models of MBL cloud and its sensitivity to  
9 environmental conditions. The Eulerian and Lagrangian sampling from CSET also provides  
10 valuable data sets for directly evaluating forecast models and General Circulation Models  
11 (GCMs) used in forecast mode.

12

13 Based on this background, the following scientific goals were set for CSET:

14

15 • *Define the evolution of the cloud, precipitation and aerosol fields in stratocumulus clouds*  
16 *as they transition into the fair-weather cumulus regimes within the subtropical easterlies*  
17 *over the northern Pacific.*

18

19 • *Examine the cloud microphysical properties and processes as a function of boundary-*  
20 *layer depth, towards assessing the relative contributions of internal processes (e.g.*  
21 *entrainment, turbulence, and drizzle) and external forcing (e.g. sea surface temperature,*  
22 *winds, and subsidence) to boundary-layer cloud-system evolution.*

23

- 1 • *Evaluate the relative importance of boundary layer deepening and precipitation*  
2 *processes in driving boundary layer decoupling and cloud breakup.*
- 3
- 4 • *Provide comprehensive case studies and integrated data sets to evaluate and improve*  
5 *process models, LES, and GCMs to describe and explain cloud system evolution in the*  
6 *trades.*

7 The observational effort included characterization of the cloud, precipitation and aerosol  
8 fields in the stratocumulus and the fair-weather cumulus regimes within the subtropical easterlies  
9 over the northern Pacific. These characterizations along trajectories were designed to aid in our  
10 understanding and simulation of the transition between the two convective regimes. The  
11 Lagrangian approach allowed us to track air masses as they flowed from colder to warmer sea  
12 surface temperatures and thus minimize uncertainties in the large-scale forcing due to horizontal  
13 advection in the lower troposphere. This approach facilitates comparison with Lagrangian model  
14 simulations and the isolation of critical physical processes operating in the cloud evolution.

15

## 16 **2. Experiment Design**

17 The NSF/NCAR GV was selected for CSET because of its range and endurance and its  
18 observational capabilities. But since the GV range is substantially reduced when flown at lower  
19 levels due to slower air speeds, the amount of time that could be flown for low-level boundary  
20 sampling was limited to about 50% of the flight time between California and Hawaii. The  
21 instrumentation used on the GV allowed for a combination of *in situ* and remote sensing  
22 observations. The remote sensing observations were used both during the boundary layer  
23 sampling and the legs flown at higher altitudes.

1                   a. *Instrumentation*

2                   A full suite of probes on the GV were used for *in situ* measurements of aerosol, cloud,  
3 precipitation, and turbulence properties. The instrumentation is listed in Table 1 and described in  
4 detail on the EOL website (<https://www.eol.ucar.edu/raf/instruments/doc/>). The GV was well-  
5 instrumented for making *in situ* characterizations of the mean and turbulent wind and  
6 thermodynamic structures below, in and above the cloud layer. Further, aerosol, cloud and  
7 precipitation observations (concentrations and size distributions) were made from the GV using  
8 several probes. The GV aerosol measurements were made using an Ultra-High Sensitivity  
9 Aerosol Spectrometer (UHSAS) that samples particles in the nominal range of 0.06-1.0 microns  
10 (but reduced to 0.075-1.0 microns for CSET). A Condensation Nuclei (CN) counter gives the  
11 total aerosol concentrations greater than a threshold of about 10 nanometers. The cloud particle  
12 size distributions were measured with a cloud droplet probe (CDP) and the precipitation sized  
13 water droplet distributions were obtained using two-dimensional optical array cloud and  
14 precipitation probes, with ranges spanning 50-3000 micron (OAP 2-DC and 2DP Probe). An  
15 important addition was the second generation Holographic Detector for Clouds (HOLODEC:  
16 Fugal and Shaw, 2009; Spuler and Fugal, 2011), a new instrument used on the GV to size cloud  
17 and drizzle droplets in the range of about 6  $\mu\text{m}$  to 1 mm and to determine the three-dimensional  
18 position of hydrometeors using digital in-line holography. The unique aspects of HOLODEC are  
19 that the sample volume measured per second (about 43  $\text{cm}^3$ ) does not depend on aircraft speed  
20 and the effects produced by shattering from the aperture edges can be identified and eliminated.  
21 Most significantly, it is possible to measure cloud droplet size distributions from individual  
22 localized sample volumes with the largest horizontal dimension being 130 mm, instead of an  
23 average over more than 10 m for optical array probes (e.g. for a measurement from CDP at 10

1 Hz), as well as to determine the positions of the droplets within that volume. Post-flight analyses  
2 of the holograms recorded at 3.3 Hz produced cloud and precipitation size distributions during  
3 CSET (Glienke et al, 2017).

4 Ozone and carbon monoxide measurements were made using the Fast Response Ozone  
5 (F03 AD) and the Carbon Monoxide (Aero-Laser VUV) instruments supported by the  
6 Community Airborne Research Instrumentation (CARI) group in Atmospheric Chemistry  
7 Observations and Modeling (ACOM) of NCAR. Upward and downward longwave and upward  
8 shortwave radiative fluxes were measured by Kipp & Zonen broadband radiometers; the  
9 HIAPER Airborne Radiation Package (HARP) provided upward and downward shortwave  
10 spectral irradiances.

11 Two key remote sensing systems used on the GV during CSET were the HIAPER Cloud  
12 Radar (HCR) developed by NCAR EOL and the High Spectral Resolution Lidar (HSRL)  
13 developed under the NSF HIAPER Aircraft Instrumentation Solicitation (HIAS). These remote  
14 sensing systems were used to define macroscopic and microscopic cloud properties as the GV  
15 flew above, below, and in the clouds. The HCR characteristics are described in Rauber et al,  
16 (2017) and in Schwartz et al. (2018). It is a pulsed Doppler radar that operates at a 94 GHz  
17 frequency (3.2 mm wavelength) and has a sensitivity of -39.6 dBZ at 1 km range. The HCR in  
18 CSET was operated with a temporal resolution of 0.5 sec, which for air speeds of the GV gives a  
19 horizontal resolution of 50-100 m. The vertical range resolution of 20 m makes the HCR ideal  
20 for observing stratocumulus and cumulus clouds and their associated precipitation structures.  
21 The first three Doppler spectra moments (reflectivity, mean Doppler velocity and spectral width),  
22 calculated using the pulse-pair technique, were displayed in real-time on the aircraft and  
23 recorded and archived for processing. In addition, the raw data that give phase and amplitude

1 from the in-phase (I) and quadrature-phase (Q) signals for each pulse were recorded and archived  
2 for each flight. These raw I and Q data were used in post processing to calculate the full radar  
3 Doppler spectrum and its first four moments (Schwartz et al. 2018).

4 A special wing pod was developed for mounting the HCR on the GV (Fig. 2). The pod  
5 design allowed a steerable reflector to extend ahead of the wing to allow for sampling both  
6 below and above the aircraft. The reflector was also actively controlled to minimize pointing  
7 errors due to pitch variations on the GV (Vivekanandan et al. 2014). Operating at 94 GHz  
8 frequency, the HCR suffers from small attenuation due to absorption by water vapor and oxygen.  
9 Corrections (less than 1 dBZ/km) were made using dropsonde data obtained during CSET, based  
10 on the method described by Ulaby (1981), when the radar is looking downward from above the  
11 clouds.

12 The HCR characterized the cloud and precipitation structures and provided a measure of  
13 cloud-top heights during both pointing directions. Its volume sampling is well suited for  
14 characterizing light precipitation--a highly-localized and variable quantity (see, e.g., Wood,  
15 2005). Aircraft-based 95-GHz radar measurements have a proven track record for advancing our  
16 understanding of the role of precipitation in MBL clouds (Vali et al., 1998; Stevens et al., 2003;  
17 Wood et al., 2011a). Ground-based and airborne cloud radars have been used to characterize the  
18 vertical velocity structure of stratocumulus clouds (e.g. Lothon et al. 2004; Ghate et al. 2010)  
19 and of shallow cumulus clouds (e.g, Geerts and Miao, 2005; Ghate et al., 2011; Wang and Geerts,  
20 2012). During non-precipitating conditions (reflectivity < -15 dBZ) when the cloud droplets have  
21 negligible fall velocity, the measured Doppler velocity corrected for the aircraft motion can be  
22 used as a proxy for the vertical air motion (Lothon et al. 2004). During precipitating conditions,  
23 either (a) the fall velocity of precipitating drops can be removed from the measured Doppler

1 velocity corrected for the aircraft motion to retrieve the vertical air motion or (b) the method  
2 proposed by Luke and Kollias (2013) that uses the higher-order moments of radar Doppler  
3 spectrum can distinguish between the echoes due to cloud droplets and drizzle drops and can be  
4 used to calculate the vertical air motion. Also, when drops larger than 1.6 mm in diameter exist  
5 in the radar sample volume, a “notch” in the Doppler spectrum can be observed (Kollias et al.  
6 2000) due to scattering by the drops in the Mie regime. The presence of the Mie notch allows the  
7 retrieval of air vertical velocity (e.g. Kollias et al, 2000; Giangrande et al 2012; Ming et al,  
8 2017). Mie notches were observed frequently during CSET and will be used to deduce vertical  
9 air motions in more heavily precipitating clouds using the HCR.

10 The HSRL used in CSET is an eye-safe calibrated lidar system that measures backscatter  
11 cross section, extinction and depolarization properties of atmospheric aerosols and clouds  
12 (Razenkov et al., 2002 and 2008). The HSRL provides estimates of cloud base heights while  
13 pointing up, and cloud top height estimates when pointing down, together with aerosol  
14 properties, derived from profiles of backscatter cross-section, extinction cross-section and  
15 depolarization ratio at 532 nm at a temporal resolution of ~0.5 sec. The range resolution of the  
16 retrieved backscatter cross-section profiles is ~30 m while that of the extinction profile is ~300 m  
17 (Morley et al., 2012). The circular depolarization ratio observed by the HSRL can aid distinction  
18 between different aerosol types based on their aspect ratio (Burton et al. 2011). On the GV the  
19 laser transmitter and telescope can be manually oriented to face either upward or downward (see  
20 Fig. 2) through windows on the top and bottom of the fuselage.

21 The first three Doppler spectral moments from the HCR, and the backscatter and  
22 extinction cross-section from the HSRL were combined to retrieve drizzle drop size distributions  
23 while pointing up using the technique proposed by O’Connor et al. (2005). For optically thin

1 clouds that were detected by both the HCR and the HSRL, the cloud drop size distributions were  
2 also retrieved (see Wood et al, 2018 for an example from a CSET flight).

3         When the aircraft was flying above the MBL in surveying mode (at a flight level of ~6  
4 km), the HCR and HSRL were operated pointing downwards to observe MBL cloud and aerosol  
5 fields from the flight level to the surface. For clouds that are 5 km below the aircraft, the HCR  
6 minimum detectable reflectivity is about -23 dBz. On flight legs below the cloud base (near  
7 surface), the HCR and HSRL were facing upwards to sample clouds and aerosols above the  
8 flight level. During the flight legs in the clouds, the HCR and HSRL were pointing downwards to  
9 characterize the sub-cloud layer aerosol and precipitating fields. The combined HCR and HSRL  
10 retrievals were used to estimate cloud boundaries for the flights flown (Schwartz et al., 2018).

11         To further complement the HCR and HSRL measurements, a multi-frequency zenith-  
12 pointing radiometer radiometer was flown to provide liquid water path (LWP) and water vapor  
13 estimates. This radiometer is similar to one used during the VOCALS project (Zuidema et al.,  
14 2012b), but in addition to four channels around the 183 GHz water vapor absorption band also  
15 included a channel in the 90 GHz window region. Such radiometers have the potential to provide  
16 an additional fundamental cloud observation that can help connect the observations to models  
17 and quantify the cloud albedo and rain susceptibilities, or how much the cloud albedo and rain  
18 vary as a function of droplet number and LWP (Terai et al., 2012; Painemal and Zuidema, 2013).  
19 Further, they can provide a geophysical constraint on lidar and radar-specific retrievals, such as  
20 simple Z-LWC relationship for non-precipitating clouds ( $\text{dBZ} < -15$ ; Frisch et al., 1998). In this  
21 particular deployment, the radiometer did not perform as well, with inconsistent brightness  
22 temperatures between different channels. This encourages more emphasis on proper pre-  
23 deployment calibration procedures for future campaigns.

1 CSET also deployed the HIAPER Atmospheric Radiation Package (HARP), measuring  
2 both upwelling and downwelling spectrally-resolved fluxes between 350 to 2200 nm with a  
3 spectral resolution of 3-8 nm. A recently-installed updated light collector optics improves the  
4 accuracy of the measurements. Although HARP was not on a stabilized platform, the aircraft  
5 motion can be accounted for under most conditions. The above-cloud downward-looking  
6 measurements at visible and near-infrared wavelengths can be combined to produce estimates of  
7 the cloud optical depth and cloud-top effective radius following the approach of Nakajima and  
8 King (1990). This provides additional insights into the evolving cloud properties, for example  
9 the relationship of the cloud top effective radius to precipitation. The upwelling broadband  
10 irradiance spanning 200-3600 nm was independently measured, and in combination with a  
11 downwelling broadband irradiance modeled on the spectral HARP irradiances, cloud albedo can  
12 be estimated.

13 Dropsondes were launched from the GV during CSET using an AVAPS<sup>TM</sup> (Airborne  
14 Vertical Atmospheric Profiling System ([https://www.eol.ucar.edu/observing\\_facilities/avaps-](https://www.eol.ucar.edu/observing_facilities/avaps-dropsonde-system)  
15 [dropsonde-system](https://www.eol.ucar.edu/observing_facilities/avaps-dropsonde-system)). *In-situ* data from the sondes were transmitted back in real time from an  
16 onboard aircraft data system via radio link. Input for times and locations of the drop releases  
17 were sent from the flight scientist on the GV to the CSET home base in Sacramento, where an  
18 operator would send instructions to the GV to trigger the sonde launches at the designated points.

#### 19 *b. Supporting tools and observations*

20 A key element of CSET was the EOL Field Catalog (see sidebar). The Field Catalog was  
21 used extensively for mission planning, real-time access to aircraft observations and satellite  
22 products during the missions, and for posting reports of mission planning, operations, and  
23 summaries. The catalog was used for documentation of the mission operations and serves as an

1 archive reference for data collected during CSET. After the mission the catalog is being used  
2 extensively in playback mode aircraft observations and ancillary products collected during each  
3 mission

4 Imagery from the 15<sup>th</sup> Geostationary Operational Environmental Satellite (GOES 15)  
5 satellite observations (centered over 135 °W longitude) was used to define the larger-scale  
6 (greater than 100 km x100 km) cloud fields using near-real-time visible and infrared images  
7 (Ch1-Ch4; and high resolution; 1km x 1km visible at nadir). Cloud property fields derived from  
8 the GOES observations were provided by the NASA Langley Satellite Cloud and Radiation  
9 Property retrieval System (SatCORPS; <https://satcorps.larc.nasa.gov>). Derived cloud properties  
10 were estimated using the methods outlined by Minnis et al. (2008) and Sun-Mack et al. (2014)  
11 and included broadband albedo, cloud-top height, cloud droplet concentrations, cloud droplet  
12 effective radius, liquid water path, and other cloud properties (see the Field Catalog Maps app  
13 for a full list). The satellite products were available in near real time from the Field Catalog and  
14 were instrumental for flight planning and for in-flight updates during the missions. All satellite  
15 product images produced during CSET are available in the playback mode with the Field Catalog  
16 Maps application.

### 17 **3. Observing Strategy and Mission Operations**

18 The general sampling strategy employed in CSET was to use the GV to sample clouds  
19 and MBL structures within trajectories extending westward along the southern periphery of the  
20 North East Pacific. This Lagrangian strategy was used to sample aerosol, cloud, and MBL  
21 properties in areas upwind from the transition zone over the North East on GV flights originating  
22 from Sacramento California and ending in Kona Hawaii. The GV and crew would then spend  
23 one day in Kona with a return flight to Sacramento two days after the outbound flight. The

1 return (inbound) flight was planned so that GV could do low-level sampling in the same air  
2 masses that were sampled two days earlier during the outbound flights. The takeoff times for the  
3 two flights in the sequence were selected so that the air masses sampled near the middle of the  
4 CA-HA track were sampled at about the same local time on both the outbound and inbound  
5 flights.

6 Two modes of operations were implemented for the GV flights. The first—a surveying  
7 mode—included radar and lidar remote sensing of the clouds and MBL from an altitude of about  
8 6 km (20 K ft) altitude along transects. In this mode, dropsondes were deployed to obtain the  
9 thermodynamic and wind structure in and above the MBL upstream and downstream from the  
10 StCu to Cu transition zone. The second—an *in situ* mode—involved detailed profiling in the sub-  
11 cloud, cloud layer, and across the top of the boundary layer in three to four selected areas  
12 upstream and downstream of the transition zone. In the surveying mode, the MBL structures,  
13 cloud properties, and aerosol distributions were sampled using the HCR and HSRL operating in  
14 a downward facing mode to sample from the flight level to the surface. This leg was typically  
15 flown at about 6 km (20 kft). Generally, *in situ* cloud and MBL observations were made in three  
16 to four targeted areas along these transects on profiling flight legs flown in and just above the BL  
17 over a distance of 1500 to 1800 km. For the return flights from Hawaii, trajectory analyses were  
18 used to identify air masses sampled two days earlier on the flight outbound from California. The  
19 flights between Sacramento California and Kona Hawaii were over a distance of about 4000 km.  
20 The CSET field phase was planned for July 1 to August 15, 2018—a time period when  
21 stratocumulus decks off the coast of California tend to be well defined.

22 Flight plans for the outbound flights originating from Sacramento were based on 500 m  
23 trajectory forecasts that were made using HYSPLIT (Hybrid Single Particle Lagrangian

1 Integrated Trajectory Model) with NCEP GFS forecasts and GDAS analyses. The trajectory  
2 forecasts used for the outbound planning comprised a swarm of 28 forward trajectories released  
3 at a height of 500 m made using the 12 UTC 0.25° forecast from the day before flight. The  
4 initial points for the 28 trajectories were subjectively chosen using the current GOES satellite  
5 visible imagery to identify areas of cloud transition and were prepared for the mission planning  
6 meetings that were held in the afternoon before an outgoing flight from Sacramento the next day.  
7 An example of a trajectory swarm forecast is shown in Fig. 3 with trajectories overlain on the  
8 GOES visible satellite imagery with the trajectory starting points for a flight planned for July 27  
9 (RF10) and a return flight on July 29 (RF11). These trajectories show the starting points (stars)  
10 and the 48-hour end points (squares) for the 28 trajectories.

11         During the mission planning meetings, the science team qualitatively examined the  
12 trajectory swarms and estimated which of the endpoints of these trajectories would be in the  
13 range of the GV on the return flight two days later. Initial points in areas where the greatest  
14 cloud cover was expected were identified as candidates for sampling on the outbound flights. On  
15 this basis, the beginning points of eight trajectories in the swarm were selected as the sampling  
16 areas on the outbound flight and the 48-hour trajectory endpoints were set as tentative sampling  
17 areas for the return flight. These flight plans were then shared with the GV pilots, who would  
18 assess the feasibility of the proposed flights and would suggest any modifications needed to  
19 make the planned flights achievable. Any model forecast errors tended to have minimal effect  
20 on the trajectory forecasts, since the position and the strength of the subtropical cyclone in the  
21 study area evolve slowly with time. But errors in the analyses used to define the initial  
22 trajectories can lead to uncertainties in the trajectory paths. A qualitative assessment of the

1 trajectories projections compared with the 48-hour movement of cloud features indicated good  
2 agreement.

3         After the GV landed in Kona , there would be another mission planning meeting the  
4 following day. During this meeting, updated trajectory end points were used to set the flight  
5 track back to Sacramento, using 12 UTC day-before-return-flight analysis and forecasts and the  
6 outbound flight path. The takeoff times for the two flights in the sequence were selected so that  
7 the air masses sampled near the middle of the CA-HI track were sampled at about the same local  
8 time on both the outbound and inbound flights. The takeoff time from CA was nominally at 8  
9 AM local time while the HI takeoff was 6:30 AM. This approach minimized diurnal effects for  
10 the middle segments of the flight. But, any diurnal effects were unavoidable for the other  
11 segments of the flight.

12         The trajectories shown in Fig. 3 define the RF10 outbound and RF11 inbound flight  
13 plans. The beginning and end points of the 8 trajectories selected for the sampling sequence are  
14 shown in Fig. 3c. These trajectories are overlaid on the satellite image from 28 July to show  
15 (after the fact) how the selected trajectories lined up with the clouds observed one day after the  
16 outgoing flight. Any minor updates to the flight plan based on subsequent forecast changes were  
17 relayed to the pilots 4 hours before takeoff based on the 06 UTC day-of-flight forecasts. For the  
18 RF10 and RF11 example sequence, the actual flight paths flown are shown in Figs 3b and 3d  
19 along with the satellite images at the different days of the aircraft operation. This same mission  
20 planning procedure was used for all of the 7 flight pairs (dates tabulated in Table 2) that were  
21 made during CSET. The detailed flight paths and field reports for each of the missions can be  
22 found in the CSET Field Catalog.

1           The basic flight pattern planned for the low-level sampling segments for all of the flights  
2 is shown in Fig. 4. The first segment started with a descent from the surveying leg at 20 k ft  
3 (about 6 km) to about 500 ft (150 m). This descent provided a pseudo-sounding, since the  
4 aircraft moves horizontally during the 20 kft descent. Then a level leg was flown at 500 ft for  
5 about 10 minutes. After this low-level leg the aircraft ascended to about 300 ft (100 m) above  
6 the cloud base for another 10 minute leg. During this leg and the 300 ft, the HCR and the HSRL  
7 beams were pointed upward. After the in-cloud leg, the aircraft would do an alternating ascent-  
8 descent sequence (saw-tooth sequence) with a vertical range of about 1500 ft (500m) to sample  
9 cloud top and the stable layer that often caps the cloud. This saw-tooth sequence was followed  
10 by a level flight leg flown 2000-3000 ft above the cloud top for about 10 minutes. During the  
11 saw-tooth and the above-cloud leg, the HCR and HSRL beams were pointed downward.  
12 Following the above-cloud leg, the aircraft descended to 500 ft and repeated the profiling  
13 sequence. The GV time-altitude plot for RF10 in Fig. 4 shows the high-level surveying legs at  
14 the beginning and the end of the flight and a sequence of four low-level profiling sequences in  
15 the mid-section of the flight. The flight plan was flexible so that modifications could be made  
16 during the aircraft sampling as dictated by local cloud and meteorology conditions.

17           Mission planning and mission control were done from the Department of Atmospheric  
18 Sciences at the University of Washington, and the aircraft home base was in Sacramento CA,  
19 where the EOL flight crew and technicians were located with the airborne mission scientists.  
20 Daily mission briefing and planning meetings were held at the University of Washington and  
21 networked to facilities at the Sacramento location and to Kona when the aircraft was there.

22           Flight operations of each mission started with preparation of the aircraft and scientific  
23 equipment about 4 hours before takeoff. The flight crew consisted of two pilots, three

1 technicians onboard the aircraft, the mission scientist and at least one additional  
2 scientist/observer. Once airborne, the mission scientist would direct the aircraft sampling  
3 sequence during the low-level profile flights and would set the dropsonde points along the  
4 surveying parts of the flight. The dropsonde points were relayed to the ground-site from where  
5 the launches were triggered. Scientists on the ground could monitor the aircraft operations and  
6 view data in near real-time along with GOES satellite products using the satellite-linked Field  
7 Catalog. A real-time communications tool (Internet Relay Chat - IRC Chat) allowed  
8 communication among the airborne scientists, engineers and technicians and CSET participants  
9 at the surface sites. These real-time exchanges facilitated any modification of the aircraft  
10 sampling areas and procedures and made full use of the many eyes that were monitoring the  
11 flights and the associated cloud conditions seen from satellite.

12 An example of the display from the Field Catalog work space (in replay mode) for the  
13 midpoint of the RF10 flight on 27 July is shown in Fig. 4b. In this depiction, the GV flight path  
14 with observed winds is plotted on the image of derived effective radius from the GOES analysis.  
15 Any of the satellite cloud products can be displayed in this same format and selected using a  
16 menu that appears on the Field Catalog display. The images from the cameras on the GV can  
17 also be viewed at the same time through the web portal to the Field Catalog. The dropsonde  
18 points can be plotted on the flight display. During the flight, these Field Catalog near-real time  
19 displays can be made using the menu to select the fields displayed with the flight tack  
20 information. In addition the Field Catalog can be used to show near-real time displays of time-  
21 height plots of the HCR and HSRL returns. Other data collected can be plotted and displayed in  
22 real time or after flights using EOL's AEROS visualization software.

23

#### 4. Observational Highlights

A wide range of boundary layer structures and aerosol, cloud, and precipitation conditions were observed during the CSET missions that captured the cloud system evolution in the Pacific trades. The cloud systems sampled included solid stratocumulus infused with smoke from Canadian wildfires, mesoscale (100-200 km) cloud-precipitation complexes, and patches of shallow cumuli in very clean environments. Ultra-clean layers were observed frequently near the top of the boundary layer and were often associated with shallow, layered veil (optically thin) clouds. The extent of aerosol, cloud, drizzle and boundary layer sampling that was made over open areas of the North Pacific along 2-day trajectories during CSET is unprecedented and will enable focused modeling and process studies of cloud system evolution and the role of aerosol-cloud-precipitation interactions in that evolution.

Synoptic conditions during CSET were typical of summertime conditions over the North East Pacific, although sea surface temperatures were slightly above normal. On average the center of the subtropical anticyclone was at about 43 N and 148 E during the CSET observing period (Fig. 5), which is slightly north of the climatological position. Some variations in the strength and location of the anticyclone were observed during the 6 weeks of observations. The sea surface temperatures (Fig. 5) in the study area were about 0.5 °C above 1981-2010 base values. The mean low-level cloudiness from the GOES estimates is shown in Fig. 6. The winds and clouds in the southern parts of the observing areas were occasionally perturbed by tropical storms and cyclones moving through or near this area. These perturbations had limited impact on the CSET observations.

During CSET a total of 7 two-flight sequences (14 research flights; RF02 to RF15; see Table 2) were flown between Sacramento and Kona during the period from July 7 to Aug 9,



1           A sample of the Lagrangian tracking of clouds and aerosols with the HCR and HSRL  
2 during the outbound RF10 (27 July 2015) and the inbound RF11 (29 July 2011) flight sequences  
3 discussed earlier (Fig. 3) are shown in Figs. 7a and 7b. The changes in the boundary layer depth  
4 with longitude are shown clearly by the HCR and HSRL returns along the outbound flight in Fig.  
5 7a where the depth increases from about 0.5 km to 1.2 km from 124° to 130° W. From 130° to  
6 137 °W the boundary layer depth is nearly constant at a height of about 1.2 km and then  
7 increases to about 2.5 km at 140°W. The cloudiness is substantially reduced west of 140° W.

8           The boundary layer is more distinctly defined by the lidar than the radar in some cases,  
9 since the survey portions of the flight were flown at a height where the radar sensitivity is  
10 insufficient to detect low non-precipitating thin clouds. But when flying below the cloud, the  
11 lidar is facing upward and does not detect cloud top in optically thick clouds. On the RF11 return  
12 flight two days later the boundary layer depth is about 1.8 km from 145 to 135 °W and then  
13 decreases to about 300 m at 125 °W. The lidar returns in this area show mesoscale variability in  
14 the time-height aerosol structure in the PBL. The top of the areas of enhanced backscatter are  
15 interpreted as the top of the boundary layer in this region.

16           The low-level sampling legs shown in Fig. 7a and 7b are segmented into the areas  
17 labeled by capital letters. The segments labeled on the outbound flight sample the beginning of  
18 the trajectories selected for the mission and the corresponding letters on the inbound flight in this  
19 case correspond to the equivalent end points of the 48-52 hour trajectories. A blowup of the lidar  
20 and the radar sampling made on the BC segments for RF10 and RF11 is shown in Fig. 8. These  
21 segments clearly show a strong change in the cloud type and amount between the beginning and  
22 the end of the trajectories. After two days there is substantially less low cloud in the end of the  
23 trajectory sampling than in the beginning. There is also a notable deepening of the boundary

1 layer from the beginning to the end of the segments. At the beginning of the trajectory sample  
2 area BC the radar indicates relatively solid cloud cover with drizzle and rain falling from the  
3 clouds. The cloud fraction from the remote sensing measurements is about 80%. On the return  
4 flight sampling at the end of the BC trajectories, there are relatively few clouds with a few weak  
5 echoes from small cumuli. The lidar returns in this area show mesoscale variability in the time-  
6 height aerosol structure in the PBL from 0.5 to 1.8 km altitude. This mesoscale variability may  
7 be due to processing of the aerosols by previous convective activity.

8           Potential temperature, mixing ratio, and wind profiles at the beginning and the end of the  
9 BC trajectory (Fig. 9) from the aircraft measurements show the evolution of the boundary layer  
10 structure over the two-day period. As expected, there is substantial warming (about a 4 K  
11 increase) and moistening (about 3 g/kg) over the period that are consistent with the increase in  
12 SST along the trajectory. The capping inversion defined from the soundings increases from about  
13 1.4 km at the beginning of the trajectory to about 2.3 km at the end. The potential temperature  
14 and mixing ratio profiles show some decoupling at the beginning of the trajectory that becomes  
15 more pronounced at the end. These profiles represent a combination of vertical and horizontal  
16 variability, making interpretation of features like the moist layer observed at the top of the  
17 boundary layer ambiguous.

18           The seven Lagrangian pairs obtained during CSET provided an unprecedented  
19 description of the evolution of the clouds and boundary layer structures in the North Pacific  
20 Trades. Although there was variability on the different days, a common feature was that on the  
21 outbound flights the boundary layer was already showing signs of decoupling in the initial  
22 sampling areas associated with stratocumulus clouds around 140W. These decoupled  
23 stratocumulus areas were followed by areas that were dominated by mesoscale cloud systems.

1 The classic broken fair-weather cumulus fields were not generally sampled on the outbound  
2 flights, but were more prevalent on the beginning of the inbound flights originating from Hawaii.  
3 Although the boundary layer values are measured in the same air mass within the Lagrangian  
4 framework, the air above the inversion may not follow this trajectory due to the wind shear that  
5 was generally present just above the boundary layer. Regardless, the CSET trajectory analyses  
6 are a rich source of information for studying the evolution of aerosols and cloud and  
7 precipitation properties in the transition process.

### 8 *b. Process Studies*

9 The CSET observations also provide an observational basis for underlying processes  
10 involved in the evolution of the boundary layer clouds. This included illumination of the role of  
11 aerosol-cloud-precipitation interactions and the role of mesoscale cloud systems in the evolution  
12 of clouds along the trajectories sampled.

13 The environments sampled during some of the CSET cases showed substantial variability  
14 in the aerosols and associated cloud characteristics. An extreme example of this variability is  
15 shown for RF02 (7 July 2015), when fires in Canada produced smoke plumes that advected into  
16 the CSET sampling area and impacted clouds as shown in Fig. 10. The effective cloud droplet  
17 radius estimates from the GOES satellite products indicate that the boundary layer clouds in the  
18 areas were affected by the smoke and showed lower effective radius values compared with those  
19 obtained in the cleaner areas to the west of the smoke affected areas. The HSRL returns on the  
20 outbound flight RF02 also show substantial aerosol structures above the boundary layer.  
21 Enhanced CO and O<sub>3</sub> concentrations in the boundary layer (Fig. 10) suggest the influence of  
22 smoke in the low-level area sampled. The *in situ* GV aerosol concentrations (labeled UHSAS in  
23 Fig. 10) and mean cloud droplet concentrations (labeled N<sub>D</sub> in Fig. 10) obtained on RF02 show

1 much higher aerosol and cloud droplet number concentrations in the eastern part of the low-level  
2 sampling areas than those to the west. For a trajectory starting area sampled on the first part of  
3 the outbound RF02 flight, the boundary layer UHSAS aerosol concentrations were about  $760 \text{ cm}^{-3}$   
4 <sup>3</sup> and the concentrations above the boundary layer are about  $450 \text{ cm}^{-3}$ . In the same air mass  
5 sampled on the return flight the boundary layer concentrations were reduced to about  $410 \text{ cm}^{-3}$   
6 and the above inversion concentrations are about  $70 \text{ cm}^{-3}$ .

7 Mesoscale cloud systems in the transition area were common features observed on the  
8 CSET flights. An example of the types of systems sampled is shown in Fig. 11. These systems  
9 generally have ‘heavy’ precipitation exceeding 10 dBZ reflectivity near the core of the systems  
10 with outflow clouds at the top of the system. The two mesoscale systems sampled with the  
11 HSRL and the HCR on the RF07 (19 July 2015) flight have horizontal dimensions of about 20  
12 km and are about 60 km apart. The GOES visible image for this time period are shown in Fig.  
13 11a. Overall the cloud pattern shown in the satellite image can be characterized as open cells  
14 like those studied in VOCALS (Wood et al., 2011b). The core of the two systems is  
15 characterized by precipitation shafts with relatively high radar reflectivity and downward  
16 motions of about  $4 \text{ ms}^{-1}$ . Clearly defined outflow areas extend from these cores near cloud top.  
17 Although the cloud tops in the cores only reach about 2 km, the precipitation from these areas  
18 can be of sufficient intensity to give rainbows that were observed from the GV when flying at  
19 low levels (example shown in Fig. 11). The precipitation cores of the systems shown in Fig. 11  
20 have a horizontal extent of about 5-15 km horizontally. The outflow areas in these mesoscale  
21 systems by the radar extend 20 to 30 km--about double that of the precipitating cloud areas.

22 The lidar and radar observations made in this case were taken while the GV was flying  
23 above the boundary layer. On the edges of the cloud away from the heavily precipitating cloud,

1 the clouds are sufficiently optically thin that aerosols below the cloud can be observed with the  
2 HSRL. On the west side of the eastern cloud system two out-flow clouds at different heights are  
3 present. Both are sufficiently optically thin that the lidar penetrates both layers in some areas.  
4 These types of mesoscale cloud systems were observed on nearly all the CSET flights and  
5 clearly indicate that these systems are fundamental to the cloudiness transition observed in the  
6 CSET study area. The CSET observations provide a unique data set for studying the heavy  
7 precipitation events observed in these clouds and the aerosol-cloud-precipitation interactions  
8 involved in these mesoscale complexes.

9         The mesoscale systems sampled are also rich in different types of aerosol-cloud  
10 interactions. A feature that was frequently observed during CSET was optically thin veil clouds  
11 that were associated with layers of very low aerosol concentrations (UHSAS concentrations  $<10$   
12  $\# \text{ cm}^{-3}$ ) near the top of the boundary layer. An example of these veil cloud layers and ultra clean  
13 layers is shown in Fig. 12 with the HSRL observations made on RF07. A full study of the veil  
14 clouds and the clean layers observed during CSET is given in Wood et al. (2018). They estimate  
15 that cloud cover associated with the veil clouds to be about 50% within the transition areas  
16 sampled during CSET. These clouds are both physically and optically thin. In addition, to the  
17 extensive lidar and radar observations during CSET, the GV made several direct penetrations of  
18 the veil clouds during CSET that allowed for a characterization of the properties of the clouds  
19 and the aerosols in the vicinity of the clouds.

20         The clean layers near cloud top are clearly shown on several of the flights (Wood et al,  
21 2018). For example, the UHSAS aerosol concentrations measured on the outbound RF 06 (7  
22 July) and inbound RF 07 (9 July) are shown in Fig. 13. On the outbound flight, the boundary  
23 layer aerosol concentrations vary between 100 to 300 per cc. By the time of the inbound flight,

1 the boundary layer aerosol concentrations have depleted to approximately 50/cc, and include a  
2 well-defined area of very low aerosol concentrations near the mean tops of clouds. The observed  
3 veil clouds and clean layers appeared to be closely coupled to mesoscale cloud systems similar to  
4 those shown in Fig. 11. A challenge will be to fully understand how the veil clouds form and  
5 their connection to the clean layers. Modeling studies are addressing these questions (Blossey  
6 and Bretherton 2017; O et al. 2018). The reduction in aerosol concentrations and deeper clouds is  
7 also reflected in larger dropsizes near cloud base, with increased sub-cloud evaporation over the  
8 warmer SSTs (Sarkar et al., 2018). The larger dropsizes will both deplete the cloud layer and  
9 weight the latent cooling profile closer to the surface, further aiding the SCT.

10 This section is intended to give a snapshot of some of the observations made during  
11 CSET. The CSET observations and the flights that were flown can be explored further by  
12 visiting the CEST Field Catalog.

### 13 5. Summary

14 CSET made substantial advancement in our characterization of the evolution of cloud  
15 systems along the southeast extent of the Pacific anticyclone and demonstrated the utility of a  
16 Lagrangian sampling strategy. Extensive cloud areas were sampled and then resampled 48 hrs  
17 later along trajectories between California and Hawaii on 7 round-trip missions involving low-  
18 level flights. These observations provide an unprecedented description of the evolution of cloud,  
19 precipitation and aerosol fields in the cloud transition within the easterlies over the northern  
20 Pacific. The observations are being used to examine key processes governing the cloud and  
21 boundary layer properties in the transition, including the roles of large scale forcing (e.g. sea  
22 surface temperature and winds) and cloud-aerosol-precipitation interactions. The CSET  
23 observations provide comprehensive case studies and integrated data sets to evaluate and

1 improve process models, LES, and GCMs to describe and explain cloud system evolution in the  
2 trades.

3 CSET demonstrated the feasibility of a Lagrangian sampling strategy with the  
4 NSF/NCAR GV aircraft to study cloud system evolution. The range, endurance, and  
5 observational capabilities of the GV make it an ideal tool for studying shallow boundary layer  
6 clouds and mesoscale cloud systems over large domains. The HCR and HSRL remote sensing  
7 capabilities on the GV were critical to the success of CSET. They provided a detailed  
8 characterization of the structure of both precipitating and non-precipitating clouds and the  
9 aerosol distributions above, below and around clouds. The observing strategy employed allowed  
10 for a low-level sampling of the boundary layer over a total flight distance of about 20,000 km  
11 and another 20,000 km of sampling made in survey mode where the radar and lidar were used to  
12 characterize clouds in the boundary layer and dropsondes were used to define boundary layer  
13 structure. There were, however, some deficiencies in the observing plan that should be  
14 addressed with in future studies of this type. First, the day two sampling of air masses will not  
15 always be in the same local time frame as the initial measurements were made. Thus, in areas  
16 where the clouds and boundary layer may exhibit substantial diurnal variability, the Lagrangian  
17 strategy may not be ideal. Second, although the Lagrangian strategy seeks to minimize the  
18 advective effects in enthalpy and moisture budgets and for modeling studies, the air above the  
19 boundary layer will generally not follow the boundary layer due to vertical wind shear just above  
20 the boundary layer.

21 CSET provided enhanced learning and teaching experiences for the undergraduate and  
22 graduate students involved directly in CSET that were enabled by the use of the Field Catalog.  
23 Although the restricted passenger space on the GV limited the number of students who could

1 actually fly on missions, the Field Catalog allowed students to follow the progress of the CSET  
2 flights in real time and examine the data as they were downloaded from the aircraft.

3 The CSET observations continue to contribute to classroom teaching and learning  
4 activities for both undergraduate and graduate students world-wide. A CSET teaching module  
5 was developed ([https://www.eol.ucar.edu/content/cset-educational-](https://www.eol.ucar.edu/content/cset-educational-module)  
6 [module;http://cseteducation.weebly.com/](http://cseteducation.weebly.com/)) that allows students to experience the activities  
7 involved in carrying out a major aircraft field deployment like CSET. This module makes heavy  
8 use of EOL's CSET Field Catalog (<http://catalog.eol.ucar.edu/cset>) in playback mode (using the  
9 EOL Field Catalog Maps application) and uses GV observations for analysis exercises that can  
10 be completed by the students. The module endeavors to have students experience the types of  
11 activities involved in the field program and includes mission planning exercises. This module  
12 can also serve as a model for future EOL related aircraft field missions.

13 In summary, CSET made substantial advancements in our characterization of the  
14 evolution of cloud systems along the southeast extent of the North Pacific anticyclone. Although  
15 substantial work is in progress to analysis and use the observations made, some general features  
16 of the cloud transformation in the trades has emerged from our initial assessments. Fig. 14  
17 shows a schematic of the cloud and boundary layer evolution between California and Hawaii  
18 observed during CSET. The boundary layer undergoes a steady deepening (top increases from  
19 500 m to 2 km) in the first 2000 km as air moves from SSTs of 14 to 28°C. This deepening is  
20 associated with decoupling of the boundary layer and increased maximum precipitation rates.  
21 The solid clouds closest to the coast give way to mesoscale precipitating shallow cumulus  
22 complexes. These complexes produce outflow clouds at the top of the boundary that evolve into  
23 optically thin veil clouds that are associated with layers of depleted aerosols (ultra clean layers).

1 The strength of the inversion decreases towards the west, although the top of the boundary layer  
2 remains at a height of about 2 km. These mesoscale complexes eventually transform to fields of  
3 cumuli that also show mesoscale organization but fewer veil clouds closer to Hawaii.

4 The observations will serve as a unique source of information for many future process  
5 and modeling studies that will lead ultimately to improved simulations of low-level clouds in  
6 global models. The observational techniques developed and demonstrated using the NSF/NCAR  
7 GV as an observing platform provides a firm basis for future studies of boundary layer cloud  
8 regimes using the GV.

9

#### 10 **Acknowledgments:**

11 A special note of thanks and appreciation goes to NCAR Earth Observing System staff  
12 supporting CSET for their efforts and support in the field. A special thanks to the GV pilots who  
13 worked diligently to accommodate our needs to make the Lagrangian flight missions possible.  
14 This research was supported by the National Science Foundation Grant AGS- 1445832 to the  
15 University of Miami, Grant AGS-1445813 to the University of Washington, and Grant AGS-  
16 1445831 to the University of Chicago V.G. was also supported by the U.S. Department of  
17 Energy's (DOE) Atmospheric System Research (ASR), an Office of Science, Office of  
18 Biological and Environmental Research (BER) program, under contract DE-AC02-06CH11357  
19 awarded to Argonne National Laboratory. We gratefully acknowledge the computing resources  
20 provided on Blues, a high-performance computing cluster operated by the Laboratory Computing  
21 Resource Center at Argonne National Laboratory. The National Center for Atmospheric  
22 Research is funded by the National Science Foundation. NCEP Reanalysis data were provided by  
23 the NOAA/OAR/ESRL PSD, Boulder, Colorado, USA, from their Web site at

1 <https://www.esrl.noaa.gov/psd/>. Satellite observations were supported by the NASA MAP and  
2 CERES programd.

3

4

5

6

7

1  
2  
3  
4  
5  
6  
7  
8  
9  
10  
11  
12  
13  
14  
15  
16  
17  
18  
19  
20  
21  
22  
23

## References

Abel et al. 2017, The role of precipitation in controlling the transition from stratocumulus to cumulus clouds in a northern hemisphere cold-air outbreak, *JAS*, doi:10.1175/JAS-D-16-0362.1.

Ackerman A. S., M. P. Kirkpatrick, D.E. Stevens, and O. B. Toon, 2004: The impact of humidity above stratiform clouds on indirect aerosol climate forcing. *Nature*, **432**, 1014–1017.

Albrecht, B. A., M. P. Jensen, and W. J. Syrett, 1995: Marine boundary layer structure and fractional cloudiness. *J. Geophys. Res.*, **100**, 14209–14222.

Albrecht, B. A., C. S. Bretherton, D. Johnson, W. H. Schubert, A. Shelby Frisch, 1995: The Atlantic Stratocumulus Transition Experiment – ASTEX. *Bull. Amer. Meteor. Soc.*, **76**, p. 889-904.

Berner, A. H., C. S. Bretherton, and R. Wood, 2011: Large-eddy simulation of mesoscale dynamics and entrainment around a pocket of open cells observed in VOCALS RF06. *Atmos. Chem. Phys.*, **11**, 10525-10540.

Berner, A. H., C. S. Bretherton, and R. Wood, 2011: Large-eddy simulation of mesoscale dynamics and entrainment around a pocket of open cells observed in VOCALS RF06. *Atmos. Chem. Phys.*, **11**, 10525-10540.

Berner, A.H., C. S. Bretherton, R. Wood, and A. Muhlbauer 2013: Marine boundary layer cloud regimes and POC formation in an LES coupled to a bulk aerosol scheme. *Atmos. Chem. Phys.*, **13**, 12549-12572, 2013.

Blossey, P. N., C. S. Bretherton, M. Zhang, A. Cheng, S. Endo, T. Heus, Y. Liu, A. Lock, S. R. de Roode, and K. M. Xu (2013), Sensitivity of marine low clouds to an idealized climate

1 change: The CGILS LES intercomparison, *J. Adv. Model. Earth Sys.*,  
2 doi:10.1002/jame.20025.

3 Bony, S. and J. L. Dufresne, 2005: Marine boundary layer clouds at the heart of tropical cloud  
4 feedback uncertainties in climate models. *Geophys. Res. Lett.* **32**, L20806.

5 Bretherton, C. S. and R. Pincus, 1995: Cloudiness and Marine Boundary Layer Dynamics in the  
6 ASTEX Lagrangian Experiments. Part I: Synoptic setting and vertical structure. *J.*  
7 *Atmos. Sci.*, **52**, 2707-2723.

8 Bretherton, C. S., P. A. Austin and S. T. Siems, 1995: Cloudiness and Marine Boundary Layer  
9 Dynamics in the ASTEX Lagrangian Experiments. Part II: Cloudiness, drizzle, surface  
10 fluxes and entrainment. *J. Atmos. Sci.*, **52**, 2724-2735.

11 Bretherton, C. S., and M. C. Wyant, 1997: Moisture transport, lower tropospheric stability and  
12 decoupling of cloud-topped boundary layers. *J. Atmos. Sci.* **54**, 148–167.

13 Bretherton, C.S., S.K. Krueger, M.C. Wyant, P. Bechtold, E. Van Meijgaard, B. Stevens, and J.  
14 Teixeira, 1999: A GCSS boundary-layer cloud model intercomparison study of the First  
15 ASTEX Lagrangian Experiment. *Bound.-Lay. Meteorol.* **93**, 341–380.

16 Bretherton, C. S., P. N. Blossey, and J. Uchida, 2007: Cloud droplet sedimentation, entrainment  
17 efficiency, and subtropical stratocumulus albedo. *Geophys. Res. Lett.*, **34**, L03813,  
18 doi:10.1029/2006GL027648.

19 Bretherton, C. S, J. Uchida, and P. N. Blossey, 2010a: Slow manifolds and multiple equilibria in  
20 stratocumulus-capped boundary layers. *Journal of Advancing Modeling Earth Systems*,  
21 **2**, Art.#14, 20 pp.

1 Bretherton, C. S., Wood, R., George, R. C., Leon, D., Allen, G., and Zheng, X., 2010b: Southeast  
2 Pacific stratocumulus clouds, precipitation and boundary layer structure sampled along  
3 20 S during VOCALS-REx, *Atmos. Chem. Phys.*, **10**, 15921-15962.

4 Bretherton, C. S., P. N. Blossey, and C. R. Jones (2013), Mechanisms of marine low cloud  
5 sensitivity to idealized climate perturbations: A single-LES exploration extending the  
6 CGILS cases, *J. Adv. Model. Earth Syst.*, *5*, 316–337, doi:10.1002/jame.20019.

7 Bretherton, C. S., and P. N. Blossey, 2017: Understanding mesoscale aggregation of shallow  
8 cumulus convection using large-eddy simulation. *J. Adv. Model. Earth. Syst.*, **9**, 2798–  
9 2821, doi:10.1002/2017MS000981.

10 Brost, R. A., D. H. Lenschow, J. C. Wyngaard, 1982a: Marine stratocumulus layers. Part 1:  
11 Mean conditions. *J. Atmos. Sci.*, **39**, 800–817.

12 Brost, R. A., J. C. Wyngaard, D. H. Lenschow, 1982b: Marine stratocumulus layers. Part II:  
13 Turbulence budgets. *J. Atmos. Sci.*, **39**, 818–836. Caldwell, P., and C. S. Bretherton, 2009:  
14 Large eddy simulation of the diurnal cycle in Southeast Pacific stratocumulus. *J. Atmos.*  
15 *Sci.*, **66**, 432-449.

16 \_de Roode, S.R., I. Sandu, J.J. van der Dussen, A.S. Ackerman, P. Blossey, D. Jarecka, A. Lock,  
17 A.P. Siebesma, and B. Stevens, 2016: Large-Eddy Simulations of EUCLIPSE–GASS  
18 Lagrangian Stratocumulus-to-Cumulus Transitions: Mean State, Turbulence, and  
19 Decoupling. *J. Atmos. Sci.*, **73**, 2485–2508, <https://doi.org/10.1175/JAS-D-15-0215.1>

20 Fang, M., B. Albrecht, E. Jung, P. Kollias, H. Jonsson, and I. PopStefanija, 2017: Retrieval of  
21 Vertical Air Motion in Precipitating Clouds Using Mie Scattering and Comparison with  
22 In Situ Measurements. *J. Appl. Meteor. Climatol.*, *56*, 537–553.

- 1 Frisch, A. S., G. Feingold, C. W. Fairall, T. Uttal, and J. B. Snider (1998), On cloud radar and  
2 microwave radiometer measurements of stratus cloud liquid water profiles, *J. Geophys.*  
3 *Res.* , 103 , 23,195–23,197, doi:10.1029/98JD01827
- 4 Fugal, J. P., and R. A. Shaw, 2009: Cloud particle size distributions measured with an airborne  
5 digital in-line holographic instrument. *Atmos. Meas. Tech. Discuss.*, **2**, 659–688,  
6 doi:10.5194/amtd-2-659-2009.
- 7 Geerts, B. and Q. Miao, 2005: The use of millimeter Doppler radar echoes to estimate vertical air  
8 velocities in the fair-weather convective boundary layer. *J. Atmos. Oceanic Technol.*, **22**,  
9 225–246.
- 10 Gerber, H., G. Frick, J.B. Jensen and J.G. Hudson, 2008: Entrainment, mixing, and microphysics  
11 in trade-wind cumulus, *J. Meteorol. Soc. Japan*, **86A**, 87-106.
- 12 Ghate, V. P., B. A. Albrecht and P. Kollias, 2010: Vertical velocity structure of non-precipitating  
13 continental boundary layer stratocumulus clouds. *J. Geophys. Res.*, **115**, D13204,  
14 doi:10.1029/2009JD013091
- 15 Ghate, V. P., M. A. Miller and L. DiPreto, 2011: Vertical velocity structure of marine  
16 boundary layer trade wind cumulus clouds. *J. Geophys. Res.*, **115**, D23201,  
17 doi:10.1029/2010JD015344
- 18 Giangrande, S. E., E. P. Luke and P. Kollias, 2012: Characterization of vertical velocity and drop  
19 size distribution parameters in widespread precipitation at ARM facilities. *J. Appl.*  
20 *Meteor. Climatol.*, **51**, 380–391.
- 21 Glienke, S., A. Kostinski, J. Fugal, R. A. Shaw, S. Borrmann, and J. Stith, 2017: Cloud droplets  
22 to drizzle: Contribution of transition drops to microphysical and optical properties

1 of marine stratocumulus clouds. *Geophys. Res. Lett.*, **44**, 8002–8010,  
2 doi:10.1002/2017GL074430.

3 Hartmann, D. L. and D. Short, 1980: On the use of earth radiation budget statistics for studies of  
4 clouds and climate. *J. Atmos. Sci.*, **37**, 1233-1250. Hartmann, M. Ockert and M.  
5 Michelson, 1992: the effect of cloud type on the earth's energy balance. *J. Clim.* 5 1281-  
6 1304. Jung, E., Albrecht, B. A., Feingold, G., Jonsson, H. H., Chuang, P., and Donaher, S.  
7 L.: Aerosols, clouds, and precipitation in the North Atlantic trades observed during the  
8 Barbados aerosol cloud experiment – Part 1: Distributions and variability, *Atmos. Chem.*  
9 *Phys.*, 16, 8643-8666, doi:10.5194/acp-16-8643-2016.

10 Kalnay, E., M. Kanamitsu, R. Kistler, W. Collins, D. Deaven, L. Gandin, M. Iredell, S. Saha, G.  
11 White, J. Woollen, Y. Zhu, M. Chelliah, W. Ebisuzaki, W. Higgins, J. Janowiak, K.C.  
12 Mo, C. Ropelewski, J. Wang, A. Leetmaa, R. Reynolds, R. Jenne, and D.  
13 Joseph, 1996: The NCEP/NCAR 40-Year Reanalysis Project. *Bull. Amer. Meteor.*  
14 *Soc.*, **77**,437–472, [https://doi.org/10.1175/1520-0477\(1996\)](https://doi.org/10.1175/1520-0477(1996)077<0437:TNYRP>2.0.CO;2)  
15 [077<0437:TNYRP>2.0.CO;2](https://doi.org/10.1175/1520-0477(1996)077<0437:TNYRP>2.0.CO;2)

16 Kazil, J., Wang, H., Feingold, G., Clarke, A. D., Snider, J. R., and Bandy, A. R., 2011: Chemical  
17 and aerosol processes in the transition from closed to open cells during VOCALS-REx,  
18 *Atmos. Chem. Phys. Discuss.*, **11**, 4687-4748, doi:10.5194/acpd-11-4687-2011, 2011.

19 Klein, S. A., and D. L. Hartmann, 1993: The seasonal cycle of low stratiform clouds. *J. Climate*,  
20 **6**, 1588–1606.

21 Klein, S., D. Hartmann and J. Norris, 1995: On the relationships among low-cloud structure, sea  
22 surface temperature and atmospheric circulation in the summertime northeast Pacific. *J.*  
23 *Climate*, **8**, p. 1140-115.

1 Kollias, P., B. A. Albrecht and F. Marks Jr. 2000: Why Mie? Accurate observations of vertical  
2 air velocities and raindrops using a cloud radar. *Bull. Amer. Meteor. Soc.*, **83**, 1471-1483.

3 Kollias, P., W. Szyrmer, J. Rémillard, and E. Luke 2011: Cloud radar Doppler spectra in  
4 drizzling stratiform clouds: 2. Observations and microphysical modeling of drizzle  
5 evolution, *J. Geophys. Res.*, **116**, D13203, doi:10.1029/2010JD015238.

6 Lilly, D. K., 1968: Models of cloud topped mixed layers under a strong inversion. *Quart. J. Roy.*  
7 *Meteor. Soc.* **94**, 292–309.

8 Lothon, M., D. H. Lenschow, D. Leon and G. Vali, 2004: Turbulence measurements in marine  
9 stratocumulus with airborne Doppler radar. *Quart. J. Roy. Meteor. Soc.*, **131**, 2063-2080

10 Luke, E.P. and P. Kollias, 2013: Separating Cloud and Drizzle Radar Moments during  
11 Precipitation Onset Using Doppler Spectra. *J. Atmos. Oceanic Technol.*, **30**, 1656–  
12 1671, <https://doi.org/10.1175/JTECH-D-11-00195.1>.

13 J. McGibbon and C. S. Bretherton, 2017: Skill of ship-following large-eddy simulations in  
14 reproducing MAGIC observations across the northeast Pacific stratocumulus to cumulus  
15 transition region, *Journal of Advances in Modeling Earth Systems*, 2017, **9**, 2, 810.

16 Mechoso, C.R., R. Wood, R. Weller, C. S. Bretherton, A. D. Clarke, H. Coe , C. Fairall, J. T.  
17 Farrar, G. Feingold, R. Garreaud, C. Grados, J. C. McWilliams , S. P. de Szoeke, S. E.  
18 Yuter, and P. Zuidema 2014: Ocean-Cloud-Atmosphere-Land Interactions in the  
19 Southeastern Pacific: The VOCALS Program. *Bull. Amer. Meteorol. Soc.*, **95**, 357-37,  
20 2014.

21 Mellado, J. P., 2010. The evaporatively-driven cloud-top mixing layer. *J. Fluid. Mech.* **660**, 5–  
22 36.

- 1 Miller, M. A., and B. A. Albrecht, 1995: Surface-Based Observations of Mesoscale Cumulus  
2 Stratocumulus Interaction during ASTEX. *J. Atmos. Sci.*, **52** (16), 2809–2826.
- 3 Minnis, P., et al. 2008: Near-real time cloud retrievals from operational and research  
4 meteorological satellites, *Proc. SPIE Int. Soc. Opt. Eng.*, **7107**, 710703,  
5 doi:10.1117/12.800344.is.etal.SPIE.abs.08.pdf.
- 6 Minor, H. A., R. M. Rauber, S. Göke, L. Di Girolamo, 2011: Trade wind cloud evolution  
7 observed by polarization radar: Relationship to giant condensation nuclei  
8 concentrations and cloud organization. *J. Atmos. Sci.*, **68**, 1075–1096.
- 9 Morley, B., S. Spuler, J. Vivekanandan, M. Hayman, E. Eloranta, 2012: Airborne and ground-  
10 based measurements with the NCAR’s GVHSRL. *16<sup>th</sup> International Symposium for the  
11 Advancement of Boundary-layer Remote Sensing*, Boulder CO. Nakajima, T. and M. D.  
12 King, 1990: Determination of the optical thickness and effective particle radius of  
13 clouds from reflected solar radiation measurements. Part I: Theory. *J. Atmos. Sci.*, **47**,  
14 p. 1878-1893.
- 15 O, K.-T., R. Wood and C. S. Bretherton, 2018: Ultraclean layers and optically thin clouds in  
16 the stratocumulus to cumulus transition: Part II. Depletion of cloud droplets and  
17 cloud condensation nuclei through collision-coalescence. *J. Atmos. Sci.*, **75**, 1653–  
18 1673, <https://doi.org/10.1175/JAS-D-17-0218.1>.
- 19 O’Connor, E.J., R.J. Hogan, and A.J. Illingworth, 2005: Retrieving Stratocumulus Drizzle  
20 Parameters Using Doppler Radar and Lidar. *J. Appl. Meteor.*, **44**, 14–  
21 27, <https://doi.org/10.1175/JAM-2181.1>

1 Neggers, R, D. Neelin and B. Stevens, 2007: Impact mechanisms of shallow cumulus convection  
2 on the tropical dynamics. *J. Climate*, **20**, 2623-2642.

3 Norris, J. R., 1998: Low cloud type over the ocean from surface observations. Part I: relationship  
4 to surface meteorology and the vertical distribution of temperature and moisture. *J.*  
5 *Climate.*, **11**, 369-382

6 Nuijens, L., B. Stevens, and A. P. Siebesma, 2009: The environment of precipitating shallow  
7 cumulus convection. *J. Atmos. Sci.*, **66**, 1962–1979.

8 Painemal, D. and P. Zuidema, 2013: The first aerosol indirect effect quantified through airborne  
9 remote sensing during VOCALS-Rex. *Atmos Chem. Phys.* **13**, pp. 917-931.  
10 doi:10.5194/acp-13-917-2013.

11 Rauber, R. M., and Coauthors, 2007: Rain in shallow cumulus over the ocean: The RICO  
12 campaign. *Bull. Amer. Meteor. Soc.*, **88**, 1912–1928.

13 Rauber, R.M., S.M. Ellis, J. Vivekanandan, J. Stith, W. Lee, G.M. McFarquhar, B.F. Jewett, and  
14 A. Janiszewski, 2017: Finescale Structure of a Snowstorm over the Northeastern United  
15 States: A First Look at High-Resolution HIAPER Cloud Radar Observations. *Bull. Amer.*  
16 *Meteor. Soc.*, **98**, 253–269, doi: 10.1175/BAMS-D-15-00180.1.

17 Razenkov, I. A., E. W. Eloranta, J. P. Hedrick, R. E. Holz, R. E. Kuehn and J. P. Garcia, 2002: A  
18 High Spectral Resolution Lidar Designed for Unattended Operation in the Arctic, 21st  
19 International Laser Radar Conference}, July 8-12, 2002, Quebec, Canada.

20 Sandu, I., and B. Stevens, 2011: On the factors modulating the stratocumulus to cumulus  
21 transitions. *J. Atmos. Sci.*, in press, doi: 10.1175/2011JAS3614.1

1 Sarkar, M, P. Zuidema, J. Jensen and B. Albrecht, 2018: Drizzle characteristics during  
2 stratocumulus-to-cumulus transition using CSET observations. (Manuscript in  
3 preparation for J. Atmos. Sci.)

4 Schwartz, M. C., V.P. Ghate, M. Cadeddu, J. Vivekanandan, S. Ellis, P. Tsai, E. Eloranta, B.  
5 Albrecht, P. Zuidema, R. Wood and C. S. Bretherton, 2018: Merged Cloud and  
6 Precipitation Dataset from the HIAPER-GV for the Cloud System Evolution in the  
7 Trades (CSET) campaign. J. Atmos. Ocean. Tech.( submitted)

8 Spuler, S. M., and J. P. Fugal, 2011: Design of an in-line, digital holographic imaging system for  
9 airborne measurement of clouds. *Appl. Opt.*, **50**, 1405–1412, doi:10.1364/AO.50.001405.

10 Sun-Mack, S., P. Minnis, Y. Chen, S. Kato, Y. Yi, S. Gibson, P. W. Heck, and D. Winker, 2014:  
11 Regional apparent boundary layer lapse rates determined from CALIPSO and MODIS  
12 data for cloud height determination. *J. Appl. Meteorol. Climatol.*, **53**, 990-1011,  
13 doi:10.1175/JAMC-D-13-081.1.

14 Soden, B. J., and G. A. Vecchi, 2011: The vertical distribution of cloud feedback in coupled  
15 ocean-atmosphere models. *Geophys. Res. Lett.*, doi:10.1029/2011GL047632

16 Stevens, B., J. Duan, J. C. McWilliams, M. Munnich and J. D. Neelin, 2002: Entrainment,  
17 Rayleigh friction and boundary layer winds over the tropical Pacific. *J. Climate*, **15**, 30–  
18 44.

19 Stevens, B., and coauthors, 2003: Dynamics and Chemistry of Marine Stratocumulus:  
20 DYCOMS-II. *Bull. Amer. Meteorol. Soc.* **84**, 579–593.

21 Teixeira, J., and co-authors, 2011: Tropical and sub-tropical cloud transitions in weather and  
22 climate prediction models: The GCSS/WGNE Pacific cross-section intercomparison  
23 (GPCI). *J. Climate*, **24**, 5223-5256.

- 1 Terai, C. R., Wood, R., Leon, D. C., and Zuidema, P., 2012: Does precipitation susceptibility  
2 vary with increasing cloud thickness in marine stratocumulus?, *Atmos. Chem. Phys.*, **12**,  
3 4567-4583, doi:10.5194/acp-12-4567-2012.
- 4 Tiedtke, M., 1989: A comprehensive mass flux scheme for cumulus parameterization in large-  
5 scale models. *Mon. Wea. Rev.*, **117**, 1779–1800.
- 6 Ulaby, F. T., R. K. Moore, and A.K. Fung, 1981: Microwave Remote Sensing: Active and  
7 Passive, Vol. I -- Microwave Remote Sensing Fundamentals and Radiometry, Addison-  
8 Wesley, Advanced Book Program, Reading, Massachusetts, 456 pp.
- 9 van der Dussen, J. J., and coauthors, 2013: The GASS/EUCLIPSE Model Intercomparison of the  
10 Stratocumulus Transition as Observed During ASTEX: LES results. *J. Adv. Model.*  
11 *Earth Syst.*, submitted 11/2012.
- 12 Vivekanandan, J., and Coauthors, 2015: A wing pod-based millimeter wavelength airborne cloud  
13 radar. *Geoscientific Instrumentation, Methods and Data Systems*, **5**, 117-159,  
14 doi:10.5194/gid-5-117-2015.
- 15 Wang, H., Feingold, G., Wood, R., and Kazil, J., 2010: Modelling microphysical and  
16 meteorological controls on precipitation and cloud cellular structures in Southeast Pacific  
17 stratocumulus, *Atmos. Chem. Phys.*, **10**, 6347-6362, doi:10.5194/acp-10-6347-2010.
- 18 Wang, Y. and B. Geerts, 2012: Composite vertical structure of vertical velocity in non-  
19 precipitating cumulus clouds. *Mon. Weath. Rev.*, Early Online Release.
- 20 Wood, R., 2005: Drizzle in stratiform boundary layer clouds. part I: Vertical and horizontal  
21 structure. *J. Atmos. Sci.*, **62**, 3011–3033.
- 22 Wood, R., 2007: Cancellation of aerosol indirect effects in marine stratocumulus through cloud  
23 thinning. *J. Atmos. Sci.*, **64**, 2657–2669.

- 1 Wood, R., C. S. Bretherton, and 32 coauthors, 2011a: The VAMOS Ocean-Cloud-Atmosphere-  
2 Land Study Regional Experiment (VOCALS-REx): goals, platforms, and field  
3 operations. *Atmos. Chem. Phys.*, **11**, 627-654.
- 4 Wood, R., C. S. Bretherton, D. Leon, A. D. Clarke, P. Zuidema, G. Allen, and H. Coe, 2011b:  
5 An aircraft case study of the spatial transition from closed to open mesoscale cellular  
6 convection over the Southeast Pacific. *Atmos. Chem. Phys.*, **11**, 2341-2370.
- 7 Wood, R., 2012: Stratocumulus clouds. *Mon. Wea. Rev.*, **140**, 2373–2423.
- 8 Wood, R. Kuan-Ting O, C. Bretherton, J. Mohrmann, B. A. Albrecht, P. Zuidema, V. Ghate, C.  
9 Schwartz, E. Eloranta, S. Glienke, R. Shaw, J. Fugal, P. Minnis, 2018: Ultraclean layers  
10 and optically thin clouds in the stratocumulus to cumulus transition: Part I. Observations.  
11 *J. Atmos. Sci.* (in press).
- 12 Wyant, M.C., C.S. Bretherton, H.A. Rand, and D.E. Stevens, 1997: Numerical simulations and a  
13 conceptual model of the stratocumulus to trade cumulus transition. *J. Atmos. Sci.* **54**,  
14 168–192.
- 15 Wyant, M. C., Wood, R., Bretherton, C. S., Mechoso, and 16 coauthors, 2010: The PreVOCA  
16 experiment: modeling the lower troposphere in the Southeast Pacific, *Atmos. Chem.*  
17 *Phys.*, **10**, 4757-4774, doi:10.5194/acp-10-4757-2010.
- 18 Yamaguchi et al. 2017, Stratocumulus to Cumulus Transition by Drizzle, JAMES,  
19 doi:10.1002/2017MS001104
- 20 Zhang, M. H. and co-authors, 2005: Comparing clouds and their seasonal variations in 10  
21 atmospheric general circulation models with satellite measurements. *J. Geophys. Res.*,  
22 **110**, D15S02, doi:10.1029/2004JD005021
- 23 Zhou, X., P. Kollias, and E. R. Lewis (2015), Clouds, precipitation and marine boundary layer

1 structure during the MAGIC Field Campaign, *J. Clim.*, **28**, 2420–2442,  
2 doi:10.1175/JCLI-D-14-00320.1.

3 Zuidema, P., Z. Li, R. Hill, L. Bariteau, B. Rilling, C. Fairall, W. A. Brewer, B. Albrecht and J.  
4 Hare, 2012a: On trade-wind cumulus cold pools. *J. Atmos. Sci.*, **69**, pp. 258-277, doi:  
5 10.1175/jas-d-11-0143.1

6 Zuidema, P., D. Leon, A. Pazmany and M. Cadetdu, 2012b: Aircraft millimeter-wave passive  
7 sensing of cloud liquid water and water vapor during VOCALS-REx. *Atmos. Chem.*  
8 *Phys.*, **12**, pp. 355-369, doi:10.5194/acp-12-355-2012.

9



1 collects any research products generated in the field that the project participants provide.  
2 Imagery that is most useful in a mapped display is ingested into the Catalog Maps tool (described  
3 below) provided that it is geo-referenced.

#### 4 **Situational Awareness and Real-Time Decision-Making:**

5 As mentioned above, the Field Catalog contains a tool called Catalog Maps, which allows users  
6 to overlay various products on a mapped display with instrument locations, flight plans, etc. This  
7 tool provides excellent situational awareness and is also available on NCAR Aircraft. Catalog  
8 Maps provides rapid updating of instrument locations, for NCAR aircraft, this update rate is  
9 currently at 5 seconds. It can show mobile vehicle locations, dropsonde and upsonde locations,  
10 winds and skewTs, aircraft tracks, satellite, radar and lightning imagery, model forecasts and  
11 other graphics.

12  
13 Other capabilities include the provision of a real-time communications tool (Internet Relay Chat  
14 - IRC Chat), expendables tracking, email product submission, objective scorecards and a  
15 preliminary data sharing service among local and remote investigators. The Field Catalog  
16 remains online prior to, during and long after the field campaign ends. The Field Catalog is  
17 developed and maintained by EOL's Data Management & Services Facility and catalogs for all  
18 current and completed field projects are available at: <http://catalog.eol.ucar.edu/>. When  
19 referencing the EOL field catalog in publications or proposals, please use the identifier  
20 link <https://doi.org/10.5065/D6SQ8XFB> .

**TABLES**

Table 1: GV Instrumentation for CSET

Instrument or Observing System	Parameters Measured and Range
Thermometer (102AL TAT)	temperature
Dewpoint Hygrometer (BUCK 1011C)	dewpoint temperature
Vertical Cavity Surface Emitting LASER Hygrometer (VCSEL)	water vapor concentration
Winds (gust measurements; aircraft motion and position)	3-D wind components
Cloud Droplet Probe (CDP)	cloud droplet spectra (2-50 $\mu\text{m}$ )
Two-Dimensional Optical Array Probe (2D-C)	cloud and drizzle droplet spectra (60-3200 $\mu\text{m}$ )
HOLODEC	cloud and drizzle (6 $\mu\text{m}$ – 1 mm)
Ultra-High Sensitivity Aerosol Spectrometer (UHSAS)	aerosol spectra (75-1000 nm)
Cloud Nuclei Counter (CN)	aerosol concentrations (>11 nm)
King probe	cloud liquid water content
Heinmann Infrared Radiation Pyrometer	sea surface temperature
Microwave Temperature Profiler (MTP)	vertical temperature profile
Broadband SW and LW Radiometers (Kipp & Zonnen)	Upward broadband shortwave irradiances, up and down infrared broadband irradiances
HIAPER Airborne Radiation (HARP)	upward and downward spectral shortwave irradiances
Digital Cameras (on right and left Wing)	forward looking images
Airborne Vertical Atmospheric Profiling System (AVAPS)	dropsonde signal processor
HIAPER Cloud Radar (HCR; 95 GHz)	reflectivity, spectral width, Doppler velocity, raw I and Q
G-Band Microwave Radiometer ( 183 GHz)	liquid water path
High Spectral Resolution LIDAR (HSRL)	backscatter and linear depolarization
Fast Response Ozone (FO3_AD)	Ozone mixing ratio
Carbon Monoxide (Aereo-Laser VUV)	carbon monoxide
Dropsondes	temp, humidity, and wind profiles

1 Table 2: Dates for research flight couplets with latitude and longitude positions of  
 2 trajectory start areas (blue circles) and end areas (red circles) 2 days later plotted in Fig 6.  
 3 Two sampling areas were identified on RF02-RF07. Three were identified on RF08-RF15.  
 4

Flight	Direction of Flight	Dates	Locations of air-masses (°N °E)	Cloud Fraction (%)
RF02	West Bound	7/7/2015	36.6, -136.7	60
			34.0, -141.6	84
RF03	East Bound	7/9/2015	28.6, -133.9	67
			27.5, -142.6	25
RF04	West Bound	7/12/2015	31.8, -130.6	97
			28.4, -137.1	71
RF05	East Bound	7/14/2015	27.9, -136.4	54
			25.0, -146.4	43
RF06	West Bound	7/17/2015	39.0, -131.5	100
			34.49, -137.0	91
RF07	East Bound	7/19/2015	27.2, -140.2	48
			25.23, -149.5	55
RF08	West Bound	7/22/2015	38.1, -128.4	69
			35.9, -132.9	100
			31.7, -138.4	72
RF09	East Bound	7/24/2015	28.3, -138.0	42
			28.1, -147.4	39
			25.1, -151.4	38
RF10	West Bound	7/27/2015	33.5, -129.6	100
			29.7, -133.9	94
			26.5, -140.0	71
RF11	East Bound	7/29/2015	28.5, -140.4	92
			27.0, -146.8	44
			23.7, -151.5	35
RF12	West Bound	8/01/2015	42.0, -130.0	44
			40.8, -134.3	47
			38.74, -138.1	50
RF13	East Bound	8/03/2015	33.5, -136.3	41
			32.2, -142.6	49
			30.02, -147.8	23
RF14	West Bound	8/07/2015	37.9, -131.9	56
			34.7, -134.7	90
			29.8, -137.8	70
RF15	East Bound	8/09/2015	28.5, -141.0	39
			26.5, -148.3	59
			23.4, -151.5	83

## FIGURE CAPTIONS

1  
2  
3  
4  
5  
6  
7  
8  
9  
10  
11  
12  
13  
14  
15  
16  
17  
18  
19  
20  
21  
22  
23  
24  
25

**Figure 1:** Photo of NSF/NCAR GV (top left) and visible GOES satellite image (top right) with aircraft path on 27 July 2015 Research Flight 10 (RF10) during CSET. The red points indicate where dropsonde launches were made. Photos from this flight were taken a camera mounted on the starboard (right) wing of the GV and shown are clouds observed along the flight path in the downstream direction (east to west) from unbroken uniform stratus (right bottom) to mesoscale complexes to shallow cumuli (left bottom).

**Figure 2:** Photos of HCR on wing of GV (top) and HSRL pointing up (bottom left) and down (bottom right) inside the GV.

**Figure 3:** Visible satellite images with trajectories used for mission planning and flight operations. White dashed line indicates great circle from Sacramento, CA to Kona, HI. a) Trajectory swarm used on July 27, 2015 for RF-10 flight planning, with GOES visible imagery from the morning of July 27; b) RF-10 flight path with dropsonde locations marked by closed circles, GOES visible imagery from morning of July 27 (day of flight); c) RF10 flight path and RF11 planning trajectories (return flight planned through squares at trajectory ends), GOES visible imagery from morning of July 28 (day between flights); d) return flight path flown for RF-11 with dropsonde locations, GOES visible imagery for July 29 (day of return flight).

**Figure 4:** a) Flight pattern plan for low-level sampling legs. Level legs are typically 8-10 minutes in duration. b) Screen shot of display from EOL Field Catalog II during RF 10; 27 July 2015 at 1042 UTC. Yellow line shows flight path with wind barbs overlain on high resolution visible GOES image and real-time photo from camera mounted on starboard (right) wing of GV.

1 **Figure 5:** Mean surface pressure, SST, and surface wind vectors for CSET (July 6-August 12)  
2 from NCAR/NCEP Reanalysis (Kalany et al. 1996). Study area is indicated by shaded areas  
3 and trajectories represent rough means of all trajectories flown.

4 **Figure 6:** Cloud fraction from GOES analyses (using Minnis et al, 2008). Blue points are  
5 starting points of trajectory sampling areas on outbound flights from Sacramento. Red points are  
6 areas sampled at end points of 48-52 hr. trajectories.

7 **Figure 7:** Figure 7: HCR reflectivity (top), HSRL backscatter (middle) and visible satellite image  
8 within 2° of the GV (bottom) for outbound RF 10 on July 27, 2015 (left) and for inbound RF-11  
9 on July 29, 2015 (right). The lettered areas in the top panels correspond to one full sequence of  
10 low-level sampling. Since flights were not made in a strictly east-west orientation, the data  
11 plotted on the longitudinal axes can be relatively compressed during parts of the flight where  
12 there might be a strong north-south component to the flight path. The GV altitude is shown by  
13 gray lines in the top and middle panels.

14 **Figure 8:** HSRL backscatter (top), HCR reflectivity (middle) and HCR Doppler velocity  
15 (bottom) for a) RF-10 segments BC at beginning of trajectories and b) RF-11 segments BC at  
16 trajectory end points. Gray lines indicate aircraft altitude.

17 **Figure 9:** Potential temperature (top left), mixing ratio (top right), wind speed (bottom left) and  
18 wind direction (bottom right) as reported by in situ instruments onboard GV during the ascents  
19 and descents made during RF10-BC and RF11-BC.

20 **Figure 10:** (a) The HSRL backscatter on outbound flight RF02 on July 7, 2015 starting at 1700  
21 UTC. (b) and (c) show the droplet effective radius from GOES analyses for the RF02 at 1600  
22 and 1800 UTC. Panels (d), (e), (f) and (g) show the UHSAS reported aerosol number  
23 concentrations, CDP reported cloud droplet number concentrations, concentration of carbon

1 monoxide, and concentration of ozone respectively. The GV track for RF02 is shown in panels  
2 (b) and (c).

3 **Figure 11:** HCR and HSRL returns from mesoscale cloud and precipitation complexes observed  
4 on RF07 (July 19, 2015) at 1910-1920 UTC. GOES high-definition visible image showing  
5 location of the aircraft near the time of the sampling. The photo of rainbow was taken on a 500  
6 ft leg at 1802 UTC (courtesy of Jonathan Emmett).

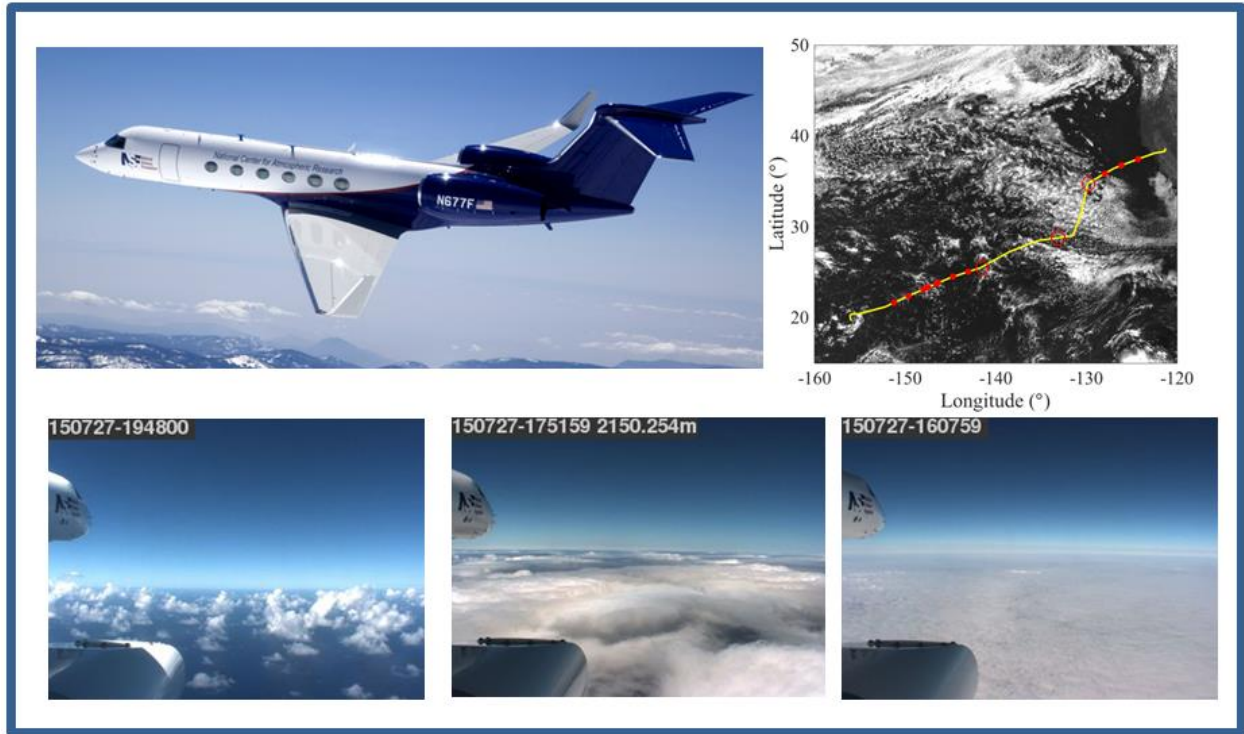
7 **Figure 12:** Optically thin veil clouds and ultra clean layers sampled from GV on July 19, 2015  
8 by HSRL starting at 1900 UTC (bottom panel). The top panels show the high resolution visible  
9 GOES image (left) and a photo taken during this time period (right). The GV track is overlaid on  
10 the satellite image with the solid line denoting the 5-min period corresponding to the HSRL plot.  
11 The photo was taken at 1907 UTC from GV.

12 **Figure 13:** UHSAS aerosol concentrations observed on outbound RF06 on July 7, 2015 (top)  
13 and inbound RF07 on July 9, 2015 (bottom) flight showing dominance of ultra clean layer  
14 (UHSAS concentration of  $<10 \text{ cm}^{-3}$ ) near cloud top on return flight RF07. The solid black lines  
15 show the cloud top heights derived from the HCR and HSRL data. Some of the UHSAS points  
16 missing below the top are from samples made within the cloud where aerosol measurements are  
17 unreliable.

18 **Figure 14:** Schematic showing cloud and boundary layer evolution from California to Hawaii  
19 from CSET perspective.

20 **Figure SB1:** CSET Field Catalog home page.

21



1  
2  
3  
4  
5  
6  
7  
8  
9  
10  
11  
12  
13

**Figure 1:** Photo of NSF/NCAR GV (top left) and visible GOES satellite image (top right) with aircraft path on 27 July 2015 Research Flight 10 (RF10) during CSET. The red points indicate where dropsonde launches were made. Photos from this flight taken from a camera mounted on the starboard (right) wing of the GV show cloud fields observed along the flight path (position of photos indicated by open red circles on GOES image) in the downstream direction (east to west) from unbroken uniform stratus (right bottom) to mesoscale complexes to shallow cumuli (left bottom).

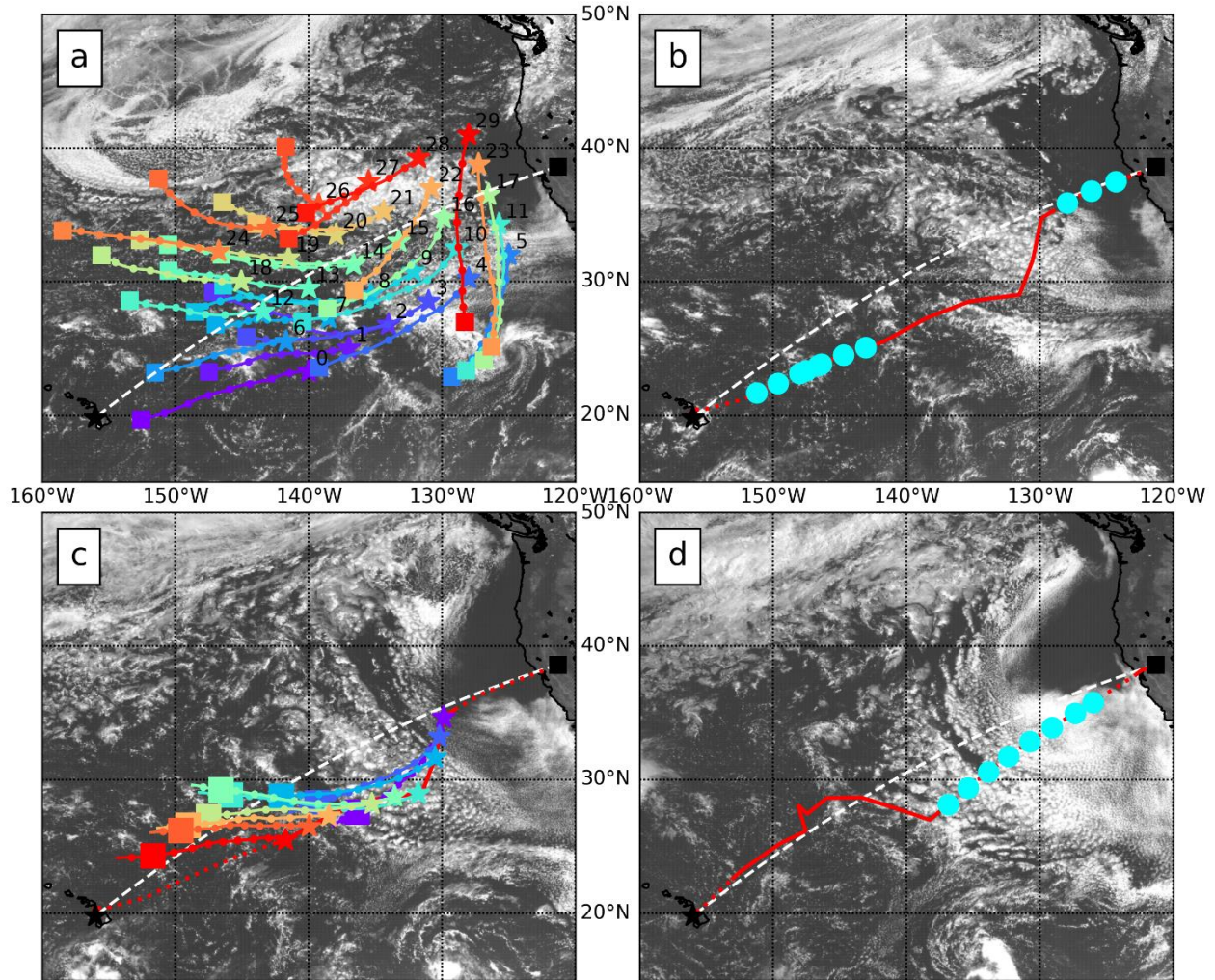


1 --

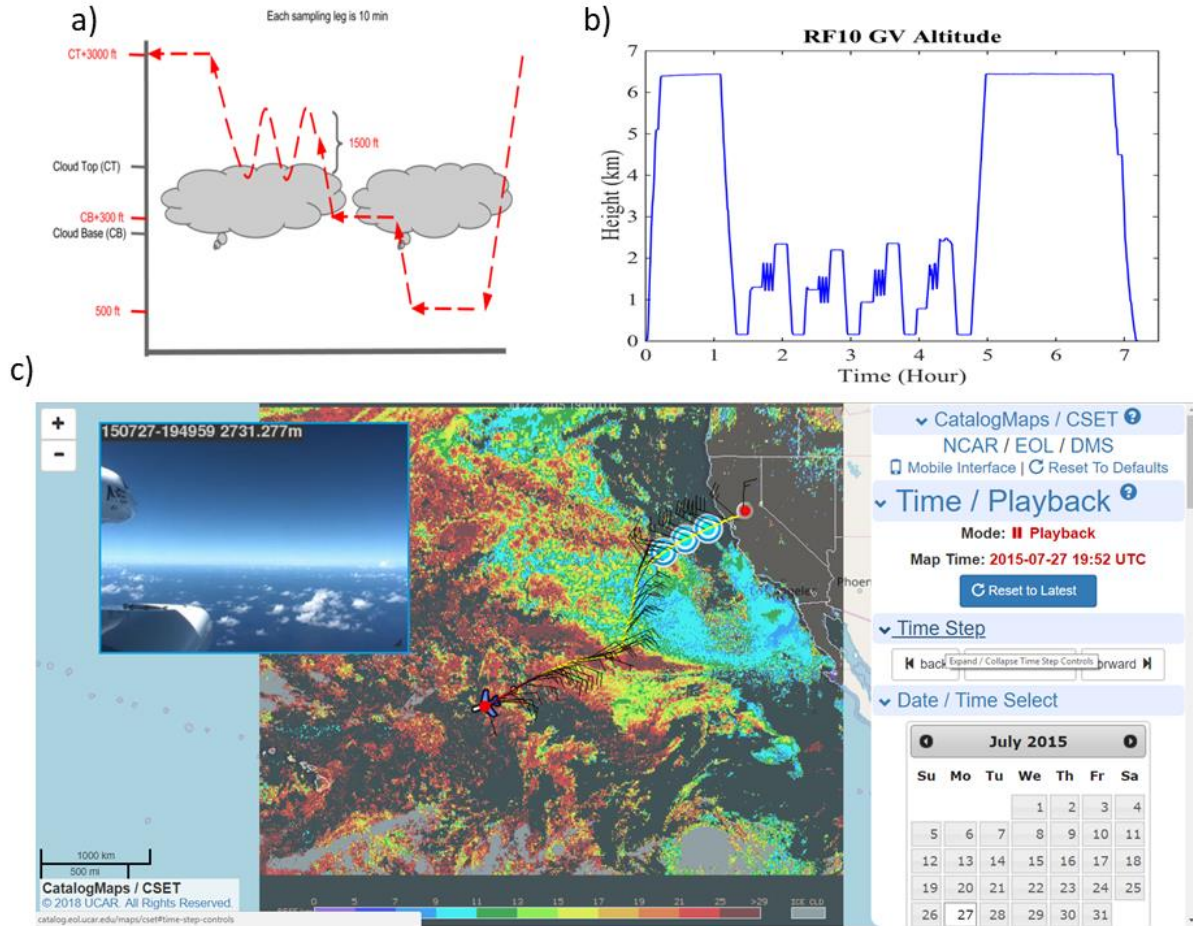
2

3

4 Figure 2: Photos of HCR on wing of GV (top) and HSRL pointing up (bottom left) and down  
5 (bottom right) inside the GV.

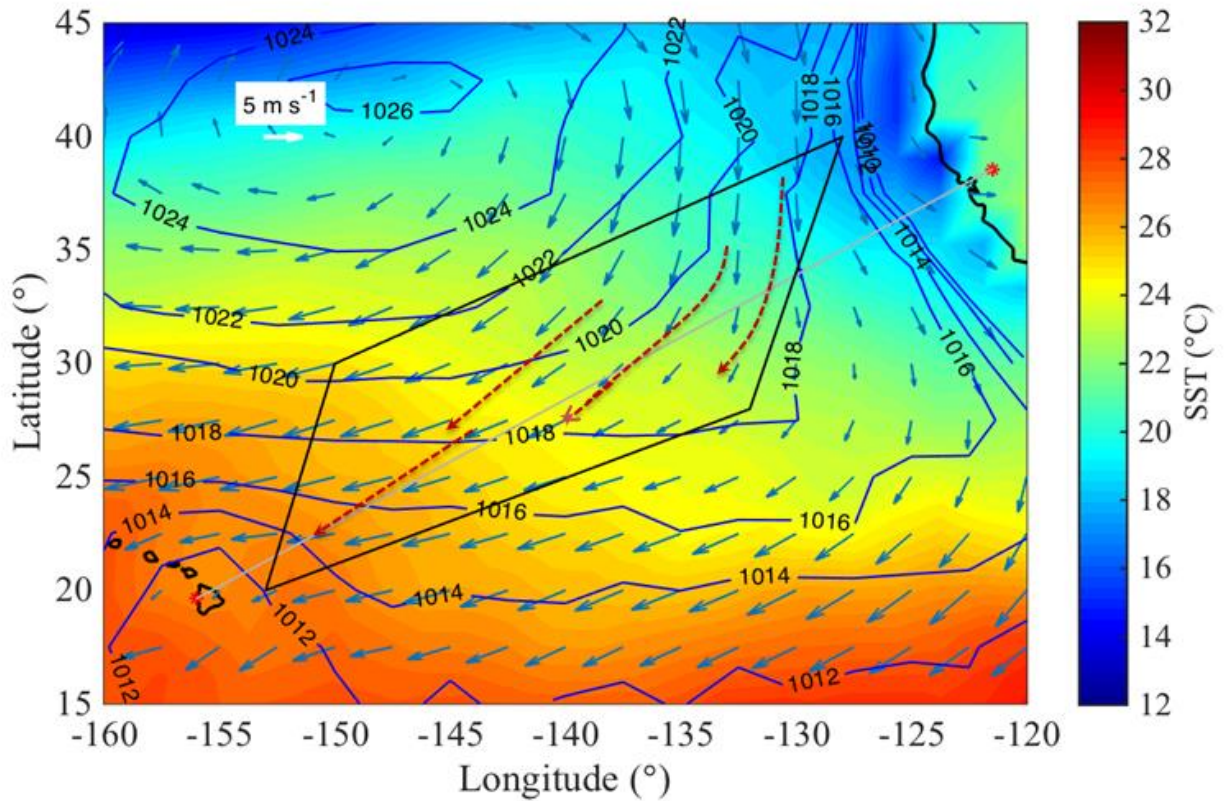


1  
 2  
 3 Figure 3: Visible satellite images with trajectories used for mission planning and flight  
 4 operations. White dashed line indicates great circle from Sacramento, CA to Kona, HI. a)  
 5 Trajectory swarm used on July 27, 2015 for RF-10 flight planning, with GOES visible imagery  
 6 from the morning of July 27; b) RF-10 flight path with dropsonde locations marked by closed  
 7 circles, GOES visible imagery from morning of July 27 (day of flight); c) RF10 flight path and  
 8 RF11 planning trajectories (return flight planned through squares at trajectory ends), GOES  
 9 visible imagery from morning of July 28 (day between flights); d) return flight path flown for  
 10 RF-11 with dropsonde locations, GOES visible imagery for July 29 (day of return flight).  
 11

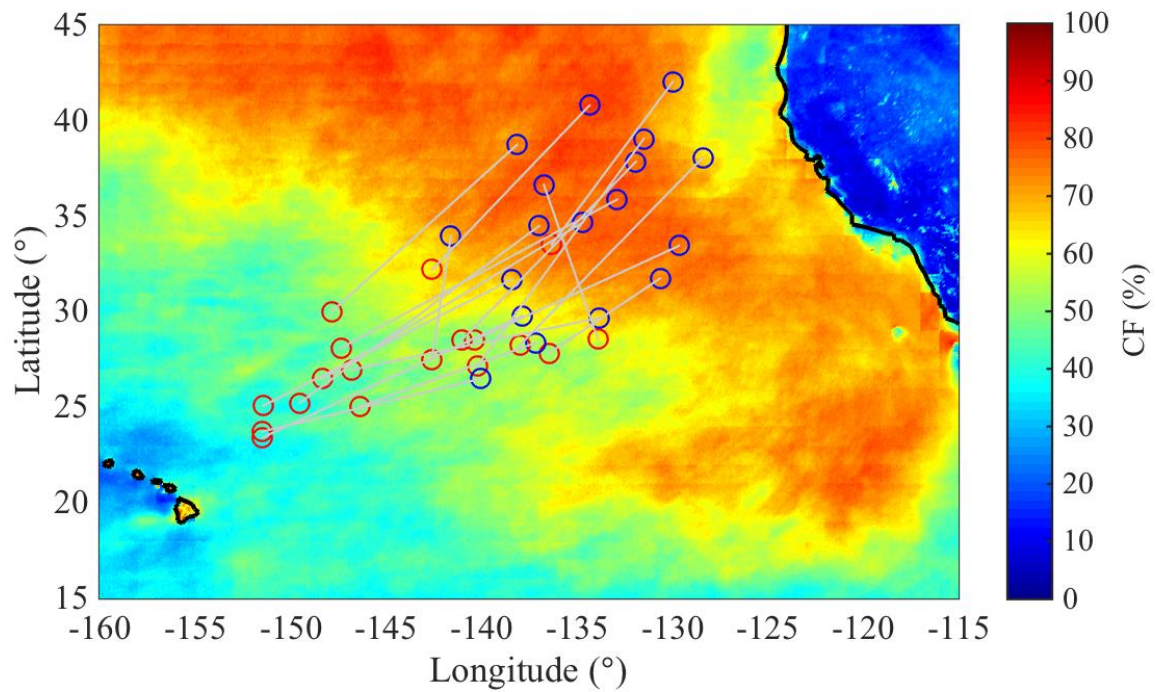


1  
2  
3  
4  
5  
6  
7  
8  
9  
10  
11

Figure 4: a) Flight pattern plan for low-level sampling legs. Level legs are typically 8-10 minutes in duration. b) Time-height plot of GV position on July 27 flight (RF10) showing the survey legs at beginning and the end of flight and the low-level sampling during the middle of the flight, and c) screen shot of computer display (in play back mode) from EOL Field Catalog II for July 27, 2015 (RF 10) at 1952 UTC. Yellow line shows flight path with wind barbs overlain on mean cloud radius from GOES analyses at this time. A time photo from camera mounted on starboard (right) wing of GV is shown for this time.



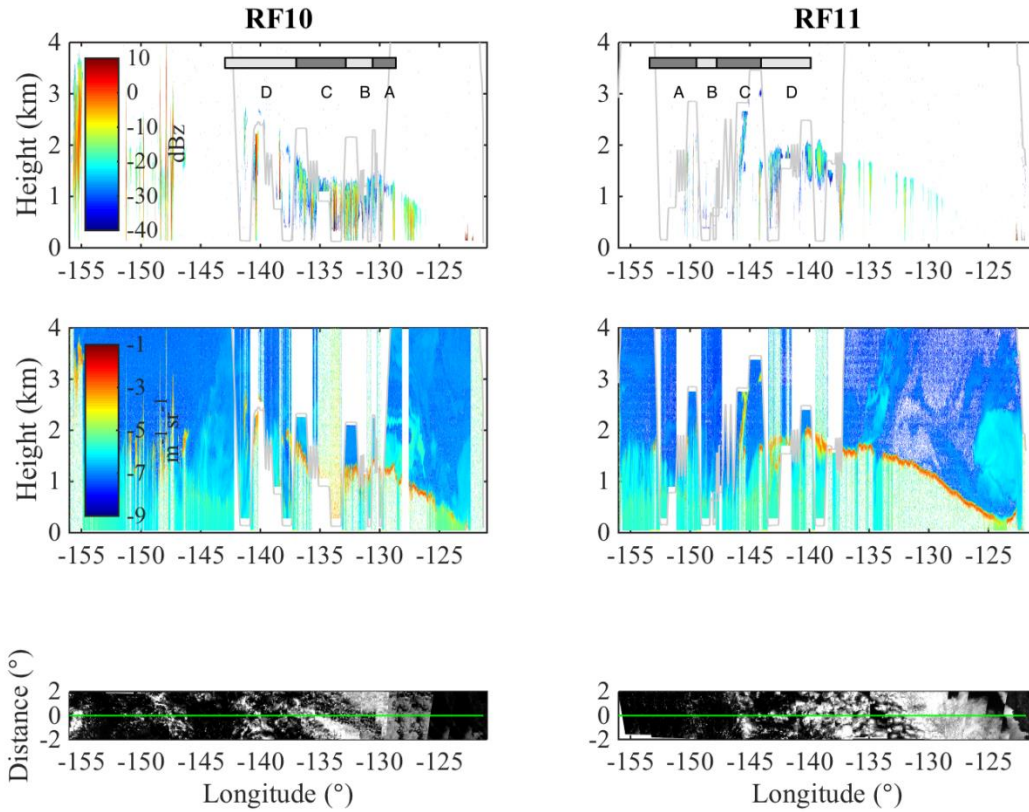
1  
 2 Figure 5: Mean surface pressure, SST, and surface wind vectors for CSET (July 6-August 12)  
 3 from NCAR/NCEP Reanalysis (Kalany et al. 1996). Study area is indicated by parallelogram and  
 4 the four trajectories represent rough means of the 48-hour trajectories used to define the  
 5 outbound study areas (beginning of the trajectories) and the inbound study areas (ends of  
 6 trajectories) sampled on all of the flights.



1  
 2 Figure 6: Cloud fraction from GOES analyses (using Minnis et al, 2008). Blue points are  
 3 starting points of trajectory sampling areas on outbound flights from Sacramento. Red points are  
 4 areas sampled at end points of 48-52 hr. trajectories on inbound flights. The locations of the  
 5 points for the areas sampled are listed in Table 2.

6  
 7  
 8

1



2

3

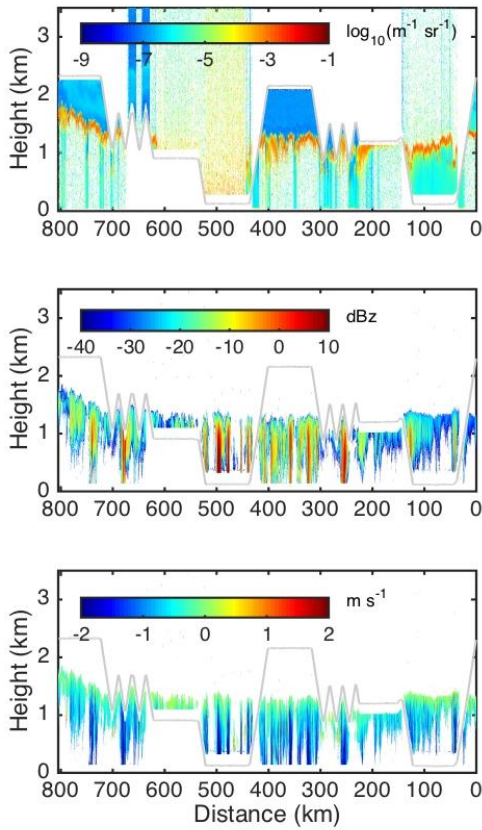
Figure 7: HCR reflectivity (top), HSRL backscatter (middle) and visible satellite image within 2° of the GV (bottom) for outbound RF 10 on July 27, 2015 (left) and for inbound RF-11 on July 29, 2015 (right). The lettered areas in the top panels correspond to one full sequence of low-level sampling. Since flights were not made in a strictly east-west orientation, the data plotted on the longitudinal axes can be relatively compressed during parts of the flight where there might be a strong north-south component to the flight path. The GV altitude is shown by gray lines in the top and middle panels.

10

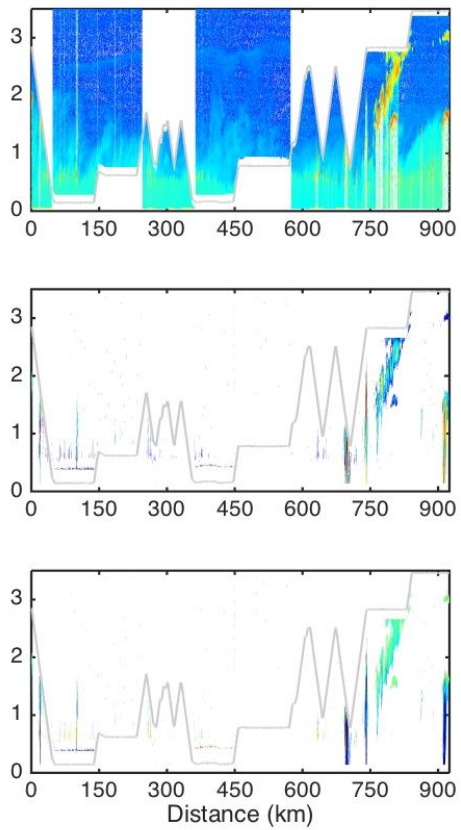
11

12

1 a)



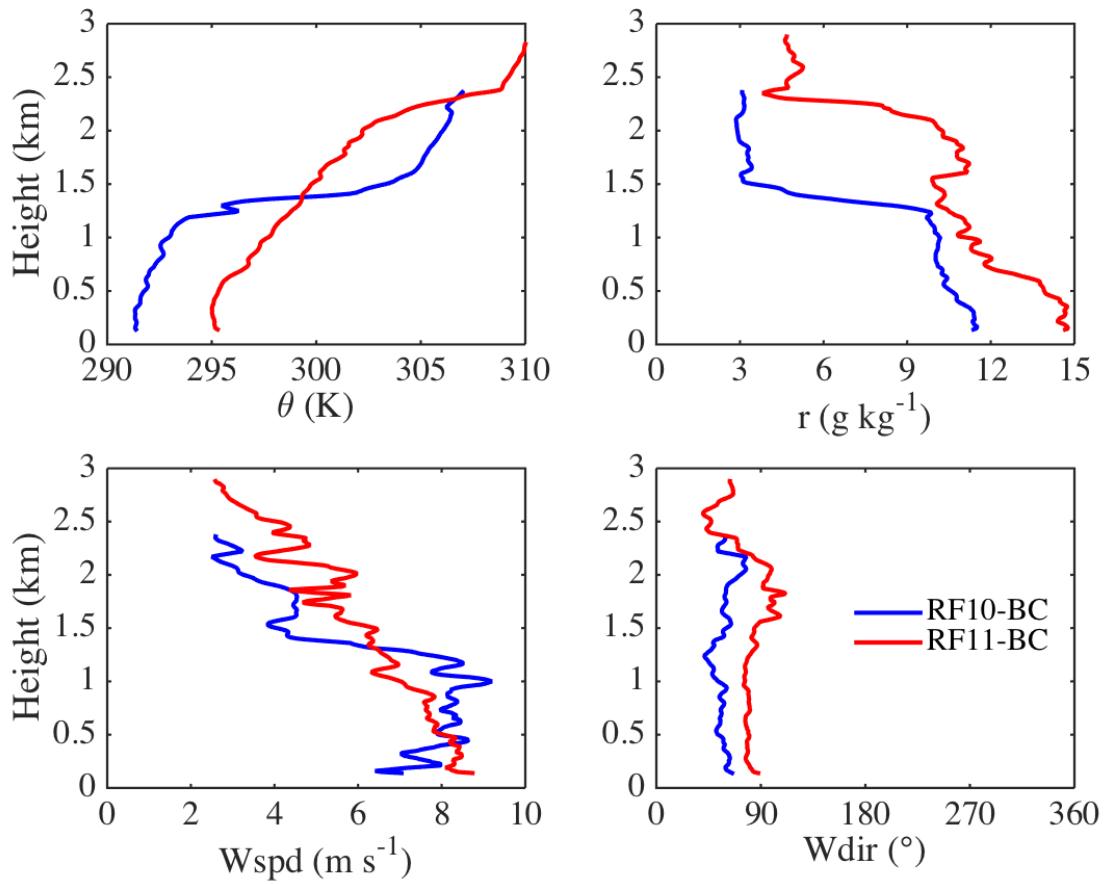
b)



2  
3 Figure 8: HSRL backscatter (top), HCR reflectivity (middle) and HCR Doppler velocity  
4 (bottom) for a) RF-10 segments BC at beginning of trajectories and b) RF-11 segments BC at  
5 trajectory end points. Gray lines indicate aircraft altitude.

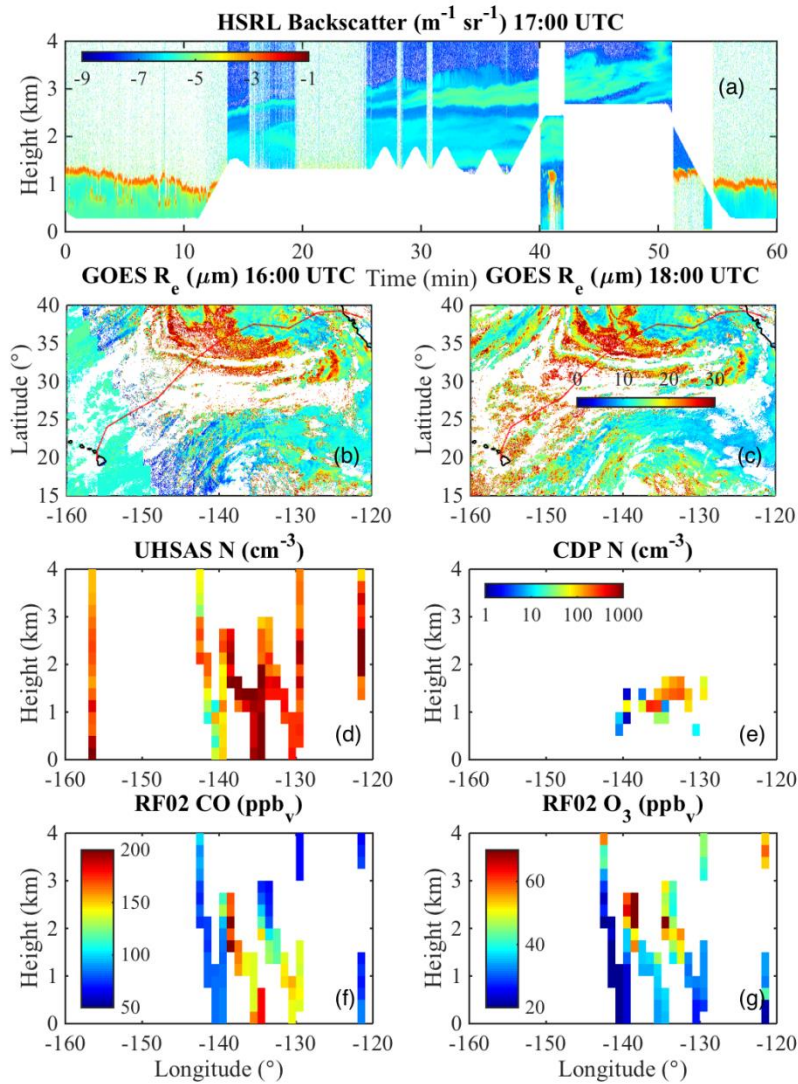
6

7



1  
2

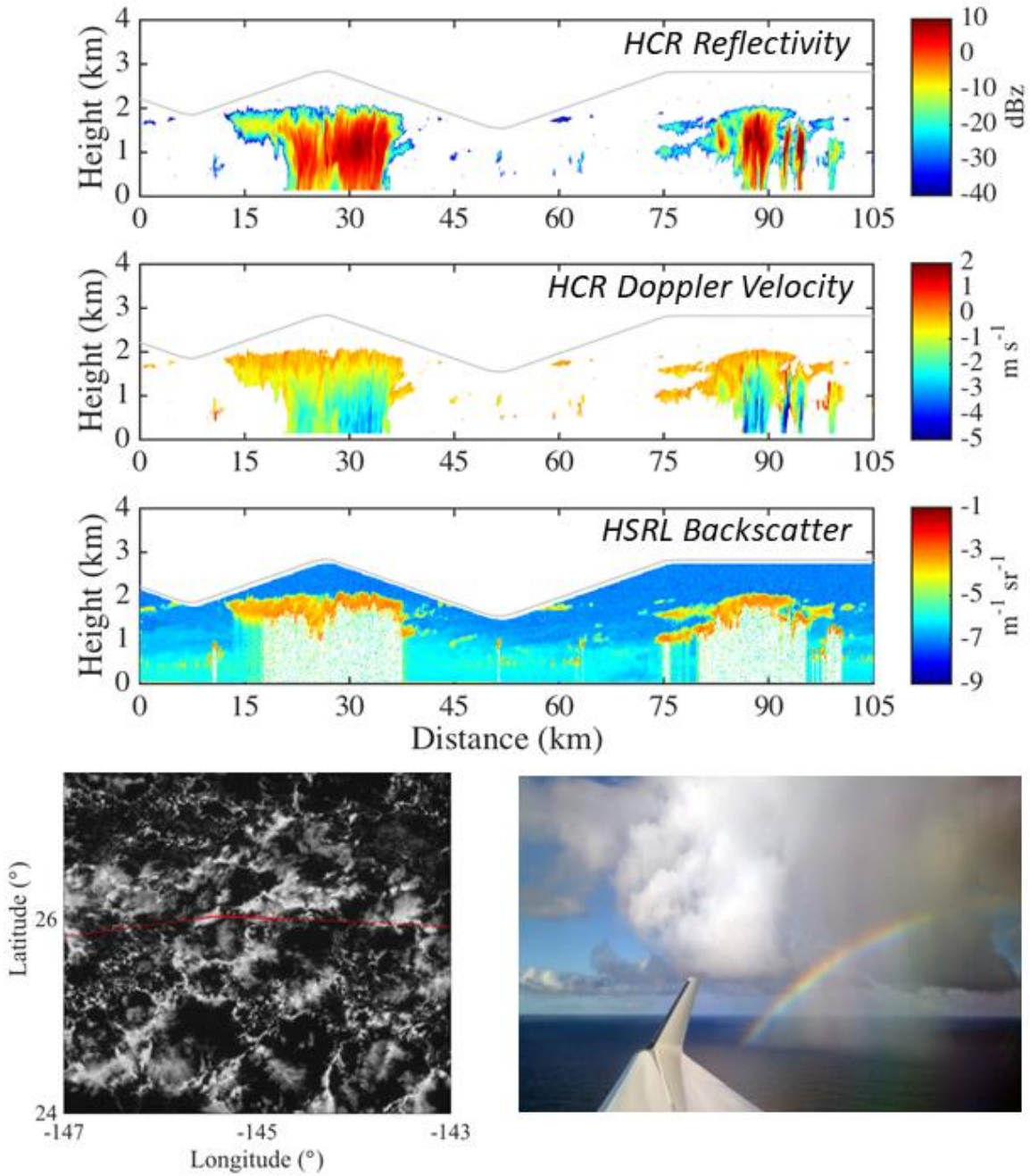
3 Figure 9: Potential temperature (top left), mixing ratio (top right), wind speed (bottom left) and  
4 wind direction (bottom right) as reported by in situ instruments onboard GV during the ascents  
5 and descents made during RF10-BC and RF11-BC.



1  
2  
3 Figure 10: (a) The HSRL backscatter on outbound flight RF02 on July 7, 2015 starting at 1700  
4 UTC. (b) and (c) show the droplet effective radius from GOES analyses for the RF02 at 1600  
5 and 1800 UTC. Panels (d), (e), (f) and (g) show the UHSAS reported aerosol number  
6 concentrations, CDP reported cloud droplet number concentrations, concentration of carbon  
7 monoxide, and concentration of ozone respectively. The GV track for RF02 is shown in panels  
8 (b) and (c).

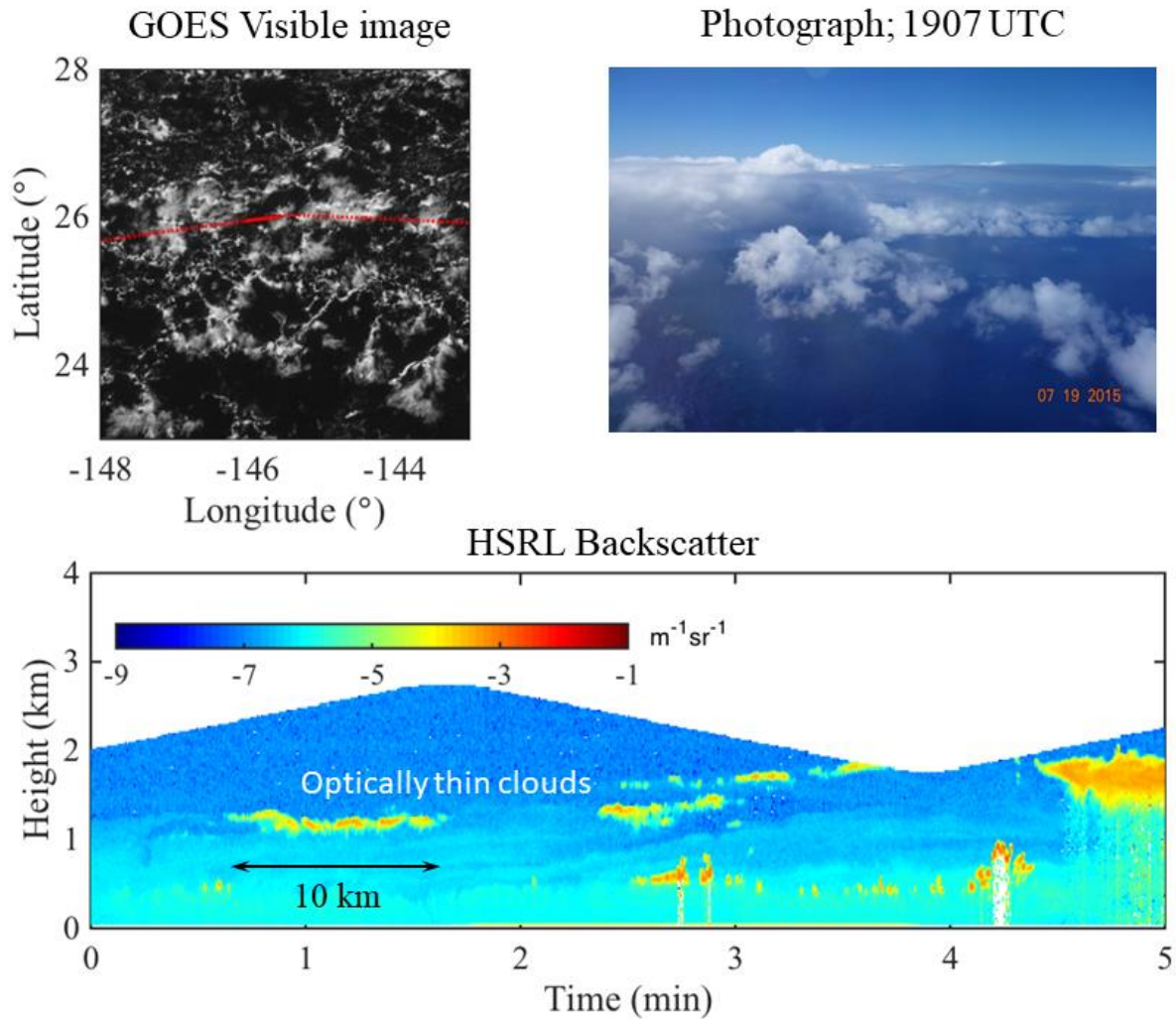
9

1  
2



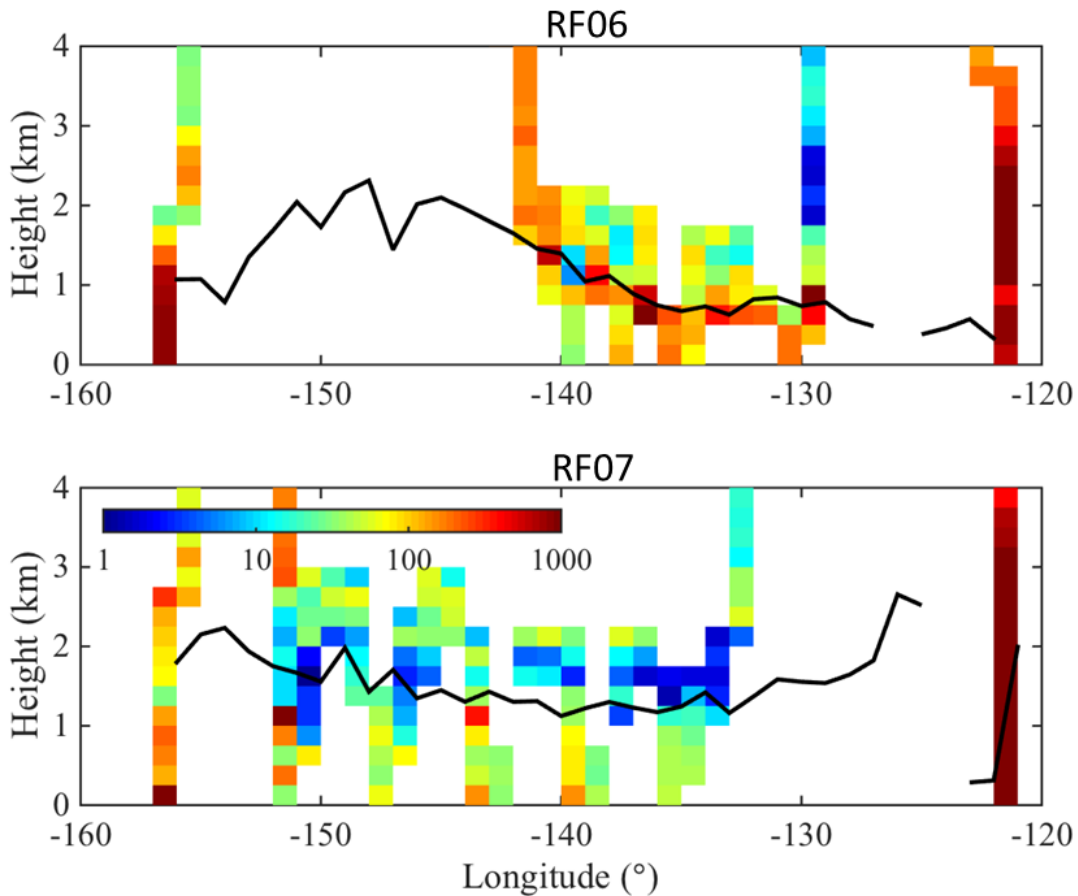
3  
4  
5  
6  
7  
8

Figure 11: HCR and HSRL returns from mesoscale cloud and precipitation complexes observed on RF07 (July 19, 2015) at 1910-1920 UTC. GOES high-definition visible image showing location of the aircraft near the time of the sampling. The photo of rainbow was taken on a 500 ft leg at 1802 UTC (courtesy of Jonathan Emmett).

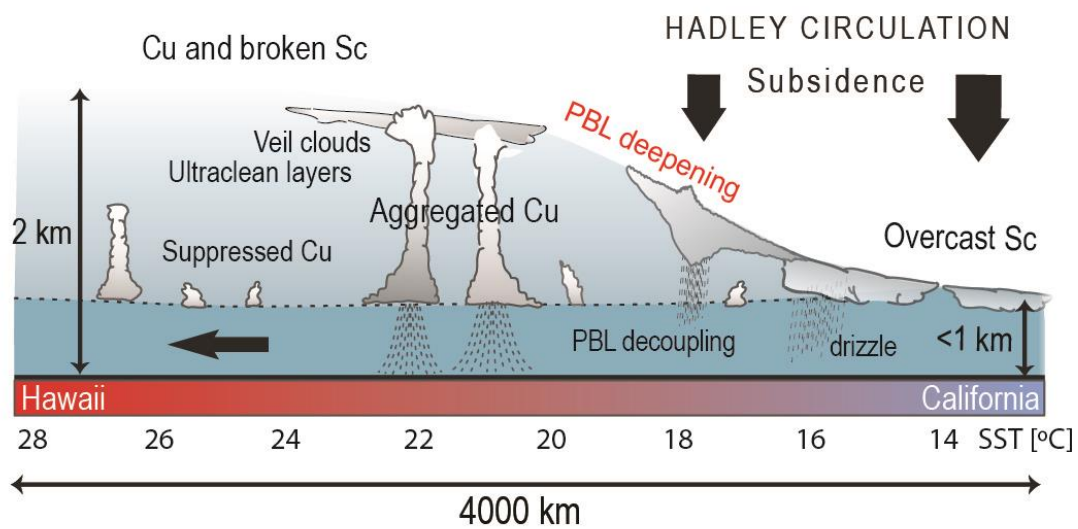


1  
2  
3  
4  
5  
6  
7  
8  
9

Figure 12: Optically thin veil clouds and ultra clean layers sampled from GV on July 19, 2015 by HSRL starting at 1900 UTC (bottom panel). The top panels show the high resolution visible GOES image (left) and a photo taken during this time period (right). The GV track is overlaid on the satellite image with the solid line denoting the 5-min period corresponding to the HSRL plot. The photo was taken at 1907 UTC from GV.



1  
 2  
 3 Figure 13: UHSAS aerosol concentrations observed on outbound RF06 on July 7, 2015 (top) and  
 4 inbound RF07 on July 9, 2015 (bottom) flight showing dominance of ultra clean layer (UHSAS  
 5 concentration of  $<10 \text{ cm}^{-3}$ ) near cloud top on return flight RF07. The solid black lines show the  
 6 cloud top heights derived from the HCR and HSRL data. Some of the UHSAS points missing  
 7 below the top are from samples made within the cloud where aerosol measurements are  
 8 unreliable.  
 9



- 1
- 2 Figure 14: Schematic showing cloud and boundary layer evolution from California to Hawaii
- 3 from CSET perspective.
- 4

**CSET Field Catalog**  
Cloud System Evolution in the Trades

Home Maps Reports Status Products Missions Tools & Links Data Access Help

**Status**

The CSET Field Campaign took place between 7/1 - 8/15/2015 over the Eastern North Pacific Ocean between the West Coast of California and Hawaii. The main base of operations for the GV was located in Sacramento, CA with a secondary base located in Kona, HI.

For a summary of these operations and related products, please click on the **"Missions"** link above.

To replay previous cases via the Field Catalog GIS tool, click on [Catalog Maps](#).

For a list of reports related to project operations, click on the **"Reports"** link above.

Datasets for this project can be found in the [CSET Data Archive at EOL](#). You can also get there via the **"Data Access"** link above.

For other data management related questions, please see the [CSET Data Management Pages at EOL](#).

Cold pools over the Pacific from Aqua

**Related Webpages**  
CSET  
EOL  
EOL/PMO

**Catalog Resources**  
Field Catalogs  
Catalog Users Guide  
Catalog Help  
Contact Us

**Social**  
EOL Facebook

© 2018 UCAR. All Rights Reserved.  
Much of the Material found on the Site is based upon work supported by the **National Science Foundation**.  
The **National Center for Atmospheric Research** is sponsored by the **National Science Foundation ("NSF")**.

1

2

3 Figure SB1: CSET Field Catalog home page.